Paradoxical Activation of Oncogenic Signaling as a Cancer Treatment Strategy

Matheus Henrique Dias[1], Anoek Friskes[2], Siying Wang[3], Joao M. Fernandes Neto[1], Frank van Gemert[4], Soufiane Mourragui[5], Chrysa Papagianni[1], Hendrik J. Kuiken[6], Sara Mainardi[1], Daniel Alvarez-Villanueva[7], Cor Lieftink[8], Ben Morris[8], Anna Dekker[1], Emma van Dijk[1], Lieke H.S. Wilms[1], Marcelo S. da Silva[9,10], Robin A. Jansen[1], Antonio Mulero-Sánchez[1], Elke Malzer[6], August Vidal[11,12], Cristina Santos[13], Ramón Salazar[13], Rosangela A.M. Wailemann[14], Thompson E.P. Torres[14,15], Giulia De Conti[1], Jonne A. Raaijmakers[2], Petur Snaebjornsson[16,17], Shengxian Yuan[18], Wenxin Qin[3], John S. Kovach[19], Hugo A. Armelin[14], Hein te Riele[4], Alexander van Oudenaarden[5], Haojie Jin[1,3], Roderick L. Beijersbergen[6,8], Alberto Villanueva[7,12], Rene H. Medema[2], and Rene Bernards[1]

ABSTRACT Cancer homeostasis depends on a balance between activated oncogenic pathways driving tumorigenesis and engagement of stress response programs that counteract the inherent toxicity of such aberrant signaling. Although inhibition of oncogenic signaling pathways has been explored extensively, there is increasing evidence that overactivation of the same pathways can also disrupt cancer homeostasis and cause lethality. We show here that inhibition of protein phosphatase 2A (PP2A) hyperactivates multiple oncogenic pathways and engages stress responses in colon cancer cells. Genetic and compound screens identify combined inhibition of PP2A and WEE1 as synergistic in multiple cancer models by collapsing DNA replication and triggering premature mitosis followed by cell death. This combination also suppressed the growth of patient-derived tumors *in vivo*. Remarkably, acquired resistance to this drug combination suppressed the ability of colon cancer cells to form tumors *in vivo*. Our data suggest that paradoxical activation of oncogenic signaling can result in tumor-suppressive resistance.

SIGNIFICANCE: A therapy consisting of deliberate hyperactivation of oncogenic signaling combined with perturbation of the stress responses that result from this is very effective in animal models of colon cancer. Resistance to this therapy is associated with loss of oncogenic signaling and reduced oncogenic capacity, indicative of tumor-suppressive drug resistance.

INTRODUCTION

Aberrant oncogenic signaling resulting from genetic and nongenetic alterations underlies the pathologic proliferation and other hallmarks of cancer (1). The last decades brought a myriad of targeted drugs to inhibit oncogenic signaling, resulting in meaningful progress in the treatment of cancer. Unfortunately, long-lasting control of advanced cancers with these agents remains virtually elusive due to the emergence of resistance (2). The pervasive heterogeneity and plasticity of advanced cancers result in the rapid selection of drug-resistant variants that have rewired cellular signaling such that the therapy becomes ineffective (3). Frequently, resistance to targeted therapies results from secondary mutations that reactivate the signaling pathway in the presence of the drug. This suggests that effective control of cancer may require approaches that are fundamentally different from the inhibition of oncogenic signaling.

There is increasing evidence that hyperactivation of oncogenic signaling can be as lethal to cancer cells as the inhibition of these pathways (4–6). A particularly compelling example is the observation that although expression of either a mutant *EGFR* or a mutant *KRAS* oncogene in the lung epithelial cells of a mouse causes cancer, their coexpression in the lung epithelium is toxic, rather than tumorigenic (7). Moreover, it is evident that oncogenic signaling in cancer cells is accompanied by an increased mobilization of stress response pathways to survive the stress associated with the oncogenic activity (8). This scenario suggests that deliberate hyperactivation of oncogenic signaling pathways in cancer cells may lead to an extreme reliance on stress response pathways, creating potential vulnerabilities. We have recently reviewed the rationale for a "paradoxical intervention" in cancer treatment and discussed how this approach can potentially address current challenges in cancer therapy (9). Such an approach consists

[1]Division of Molecular Carcinogenesis, Oncode Institute, The Netherlands Cancer Institute, Amsterdam, the Netherlands. [2]Division of Cell Biology, Oncode Institute, The Netherlands Cancer Institute, Amsterdam, the Netherlands. [3]State Key Laboratory of Oncogenes and Related Genes, Shanghai Cancer Institute, Renji Hospital, Shanghai Jiao Tong University School of Medicine, Shanghai, China. [4]Division of Tumor Biology and Immunology, The Netherlands Cancer Institute, Amsterdam, the Netherlands. [5]Hubrecht Institute-KNAW (Royal Netherlands Academy of Arts and Sciences) and University Medical Center, Utrecht, the Netherlands. [6]Division of Molecular Carcinogenesis, The Netherlands Cancer Institute, Amsterdam, the Netherlands. [7]Chemoresistance and Predictive Factors Group, Program Against Cancer Therapeutic Resistance (ProCURE), Catalan Institute of Oncology (ICO), Oncobell Program, Bellvitge Biomedical Research Institute (IDIBELL), L'Hospitalet del Llobregat, Barcelona, Spain. [8]Division of Molecular Carcinogenesis, NKI Robotic and Screening Center, The Netherlands Cancer Institute, Amsterdam, the Netherlands. [9]Department of Biochemistry, Institute of Chemistry, University of São Paulo, São Paulo, SP, Brazil. [10]Department of Chemical and Biological Sciences, Institute of Biosciences, São Paulo State University (UNESP), Botucatu, SP, Brazil. [11]Department of Pathology, University Hospital of Bellvitge, Bellvitge Biomedical Research Institute (IDIBELL), L'Hospitalet de Llobregat, Barcelona, Spain. [12]Xenopat S.L., Parc Cientific de Barcelona (PCB),

Barcelona, Spain. [13]Department of Medical Oncology, Catalan Institute of Oncology (ICO), Oncobell Program, Bellvitge Biomedical Research Institute (IDIBELL), CIBERONC, Barcelona, Spain. [14]Center of Toxins, Immune-response and Cell Signaling, Instituto Butantan, São Paulo, Brazil. [15]Department of Clinical and Experimental Oncology, Federal University of São Paulo (UNIFESP), São Paulo, Brazil. [16]Department of Pathology, The Netherlands Cancer Institute, Amsterdam, the Netherlands. [17]University of Iceland, Faculty of Medicine, Reykjavik, Iceland. [18]The Third Department of Hepatic Surgery, Eastern Hepatobiliary Surgery Hospital, Shanghai, China. [19]Lixte Biotechnology Holdings, Inc., Pasadena, California.

Deceased.

Corresponding Author: Rene Bernards, Division of Molecular Carcinogenesis, Netherlands Cancer Institute, Plesmanlaan 121, 1066 CX Amsterdam, the Netherlands. E-mail: r.bernards@nki.nl
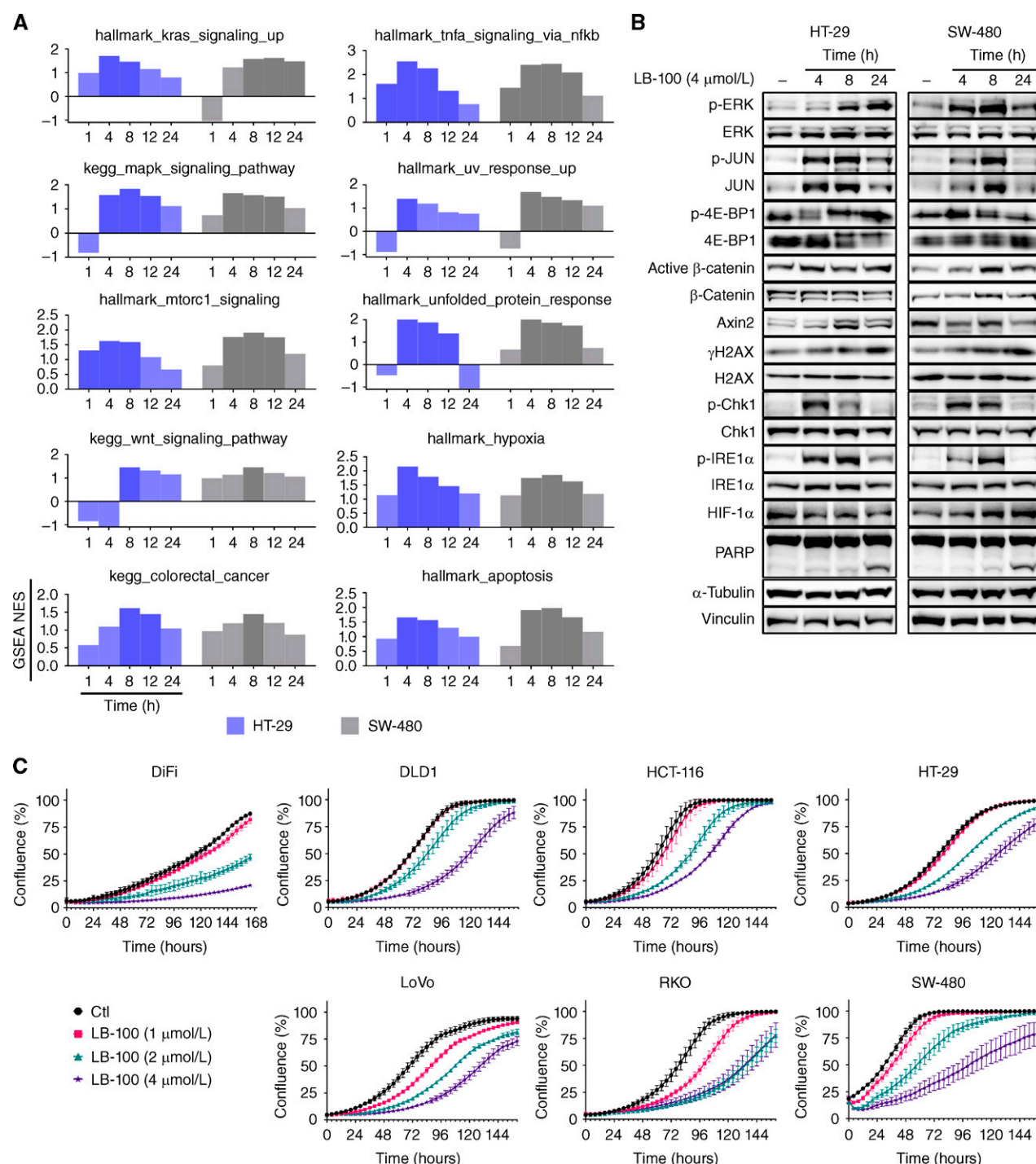
Figure 1. LB-100 activates oncogenic signaling, engages stress response pathways, and restrains the proliferation of colorectal cancer cells. **A**, Gene set enrichment analyses on time-course transcriptome data from HT-29 and SW-480 cells show selected "Hallmarks" and "KEGG" molecular signatures modulated by LB-100 (4 μmol/L). Darker bars indicate time points for which the respective gene set was significantly enriched (P <0.05). **B**, Time-course western blots show selected oncogenic signaling and stress response pathways modulated by LB-100 (4 μmol/L) in HT-29 and SW-480 cells. α-Tubulin and Vinculin were used as loading controls. **C**, IncuCyte-based proliferation assays with the colorectal cancer models in the absence or presence of LB-100 at 1, 2, or 4 μmol/L for the indicated times. (*continued on next page*)

of hyperactivation of oncogenic signaling combined with the targeting of specific stress response pathways.

Although there is a vast arsenal of drugs to inhibit oncogenic signaling, the options for hyperactivation of oncogenic signaling are more limited. The Protein Phosphatase 2A (PP2A) is a serine/ threonine phosphatase that acts in multiple cancer-relevant pathways, including mitogenic signaling, DNA damage response, and apoptosis (10–12). Evidence that

Figure 1. *(Continued)* **D,** String network combining all hits identified by the two independent genome-wide CRISPR screens (Supplementary Fig. S2) as modulators of LB-100 toxicity. Only high-confidence interactions are shown and disconnected nodes are omitted. Green nodes: CRISPRa screen; orange nodes: CRISPR-KO screen; yellow node: identified on both screens. **E,** GO analyses using the full list of hits from both CRISPR screens (Supplementary Fig. S2) as input. The top 5 enriched Biological Processes and Molecular Functions terms are shown. Darker bars highlight WNT/β-catenin-and MAPK-related terms.
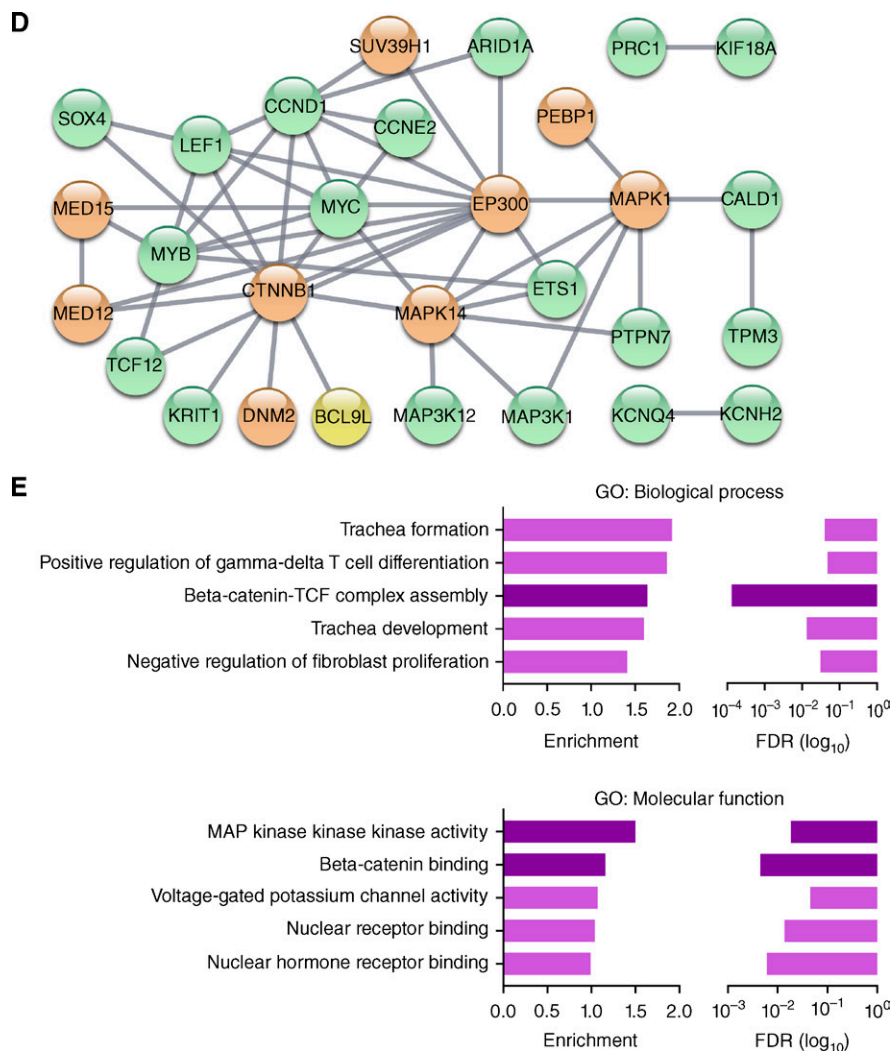
PP2A acts as a tumor suppressor in certain contexts by restraining oncogenic signaling has sparked the generation of drugs to reactivate the enzyme (13). As activation of PP2A inhibits oncogenic signaling, its inhibition should further activate these pathways. LB-100, a small-molecule inhibitor of PP2A, has shown toxicity in various cancer models. Activation of mitogenic signaling and engagement of stress response pathways have been associated with these anticancer effects (14, 15). Importantly, in a phase I clinical trial, LB-100 showed a rather favorable toxicity profile in doses associated with clinical response (16). This set of characteristics makes LB-100 an attractive drug to test the concept of paradoxical activation of oncogenic signaling for the treatment of cancer.

Using colorectal cancer cells as primary models, we show here that LB-100 hyperactivates multiple oncogenic signaling pathways and simultaneously engages several stress response pathways. Concomitant inhibition of the WEE1 kinase and PP2A is highly lethal in multiple cancer models and suppresses tumor growth *in vivo*. Most strikingly, we found that acquired resistance to this drug combination was associated with loss of the tumorigenic phenotype.

RESULTS

LB-100 Activates Mitogenic Signaling and Engages Stress Response Pathways

We focused on colorectal cancer models to test the notion that the PP2A inhibitor LB-100 further activates oncogenic signaling. We selected a panel of seven colorectal cancer cell lines carrying diverse oncogenic mutations (*KRAS, BRAF, APC, TP53, CTNNB1,* and others; Supplementary Table S1; ref. 17). Dose-response assays showed moderate toxicity of LB-100 in these colorectal cancer models, with IC$_{50}$ values varying from 1.5 to 7.2 µmol/L (Supplementary Fig. S1A).

Although we aimed to use LB-100 to activate mitogenic signaling and engage stress response pathways, PP2A phosphatases have multiple targets (12) and their inhibition likely has broader effects on cellular processes. To gain a comprehensive insight into the cellular processes modulated by LB-100, we treated HT-29 and SW-480 colorectal cancer cells with a sublethal concentration of LB-100 (4 µmol/L) for 1, 4, 8, 12, or 24 hours and performed RNA sequencing assays. We used gene set enrichment analyses (GSEA) to compare these treated samples to their respective untreated controls. We focused the analyses
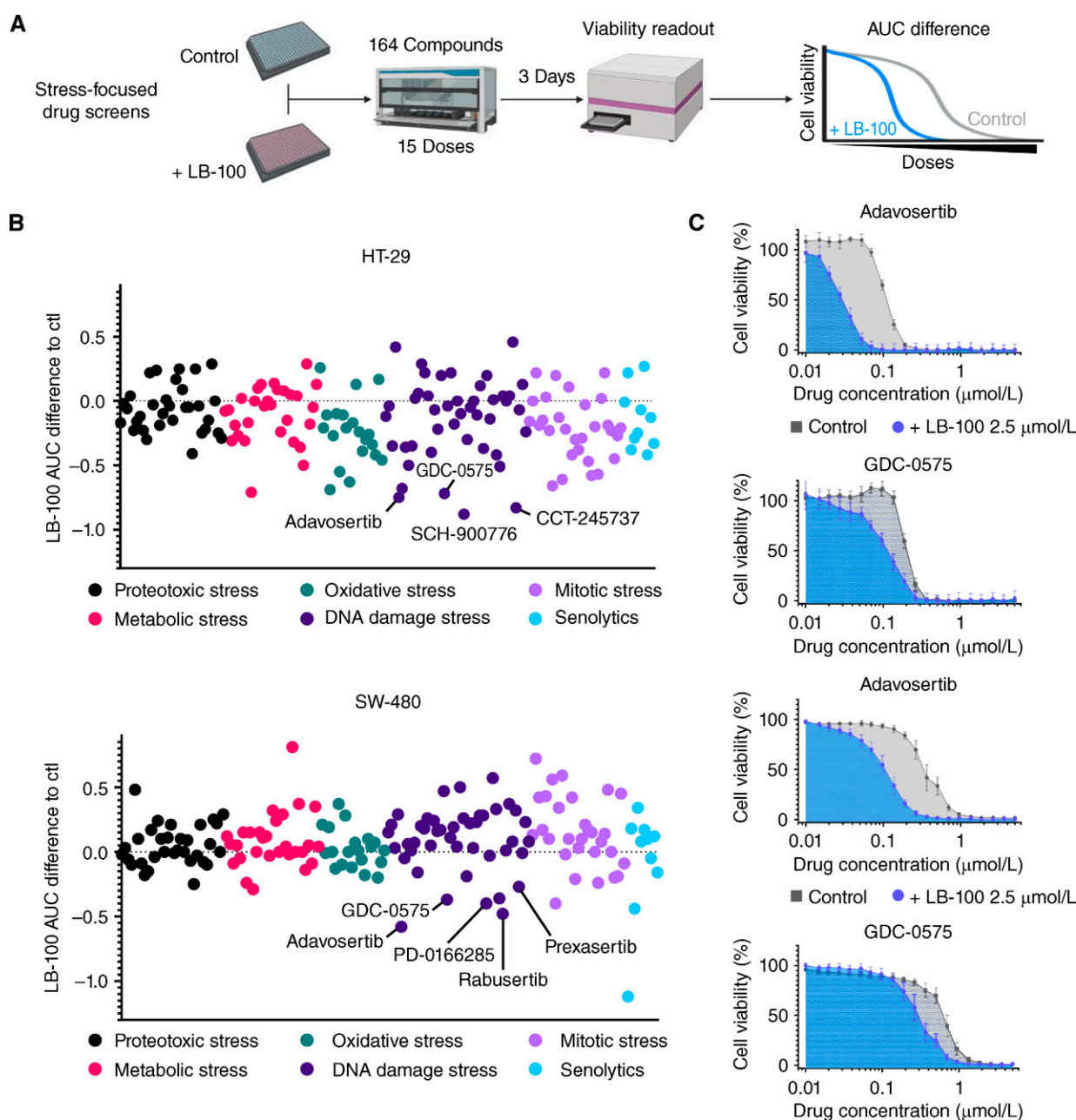
Figure 2. Stress-focused drug screen and genome-wide CRISPR screen converge to identify synthetic lethality between LB-100 and WEE1 inhibition. **A,** Schematic outline of the stress-focused drug screen. **B,** AUC difference for each compound in the presence of LB-100 (2.5 µmol/L) relative to untreated controls in HT-29 and SW-480 cells. In both cases, WEE1 and CHK1 inhibitors are annotated. **C,** Dose–response curves comparing the normalized AUC for adavosertib or GDC-0575 in the presence or absence of LB-100 (2.5 µmol/L) in HT-29 and SW-480 cells. Cell viability was estimated by resazurin fluorescence after 3 days in the presence of the drugs. (*continued on next page*)

on the "hallmark" and "KEGG" molecular signatures to cover a wide range of biological states or processes. Figure 1A (left) shows that LB-100 induces a transient positive enrichment in KRAS, MAPK, mTORC1, and WNT gene sets in both colorectal cancer models and the KEGG colorectal cancer gene set. These data corroborate that LB-100 further activates oncogenic pathways in colorectal cancer cells. Positive enrichment of gene sets associated with NF-κB signaling, UV response (DNA damage), unfolded protein response (UPR), hypoxia, and apoptosis are also seen (Fig. 1A, right), indicating the engagement of different

stress response pathways in response to LB-100. Supplementary Fig. S1B shows the remaining hallmark and KEGG gene sets found significantly enriched in at least one time point in both cell lines. Overall, gene sets related to mitogenic signaling, stress pathways, and inflammatory response pathways were positively enriched upon LB-100 treatment.

We performed a series of Western blots to validate the findings of the transcriptome analyses. Figure 1B shows that LB-100 treatment further activated the MAPK pathway as evidenced by increases in p-ERK and p-JUN in both cell lines. A
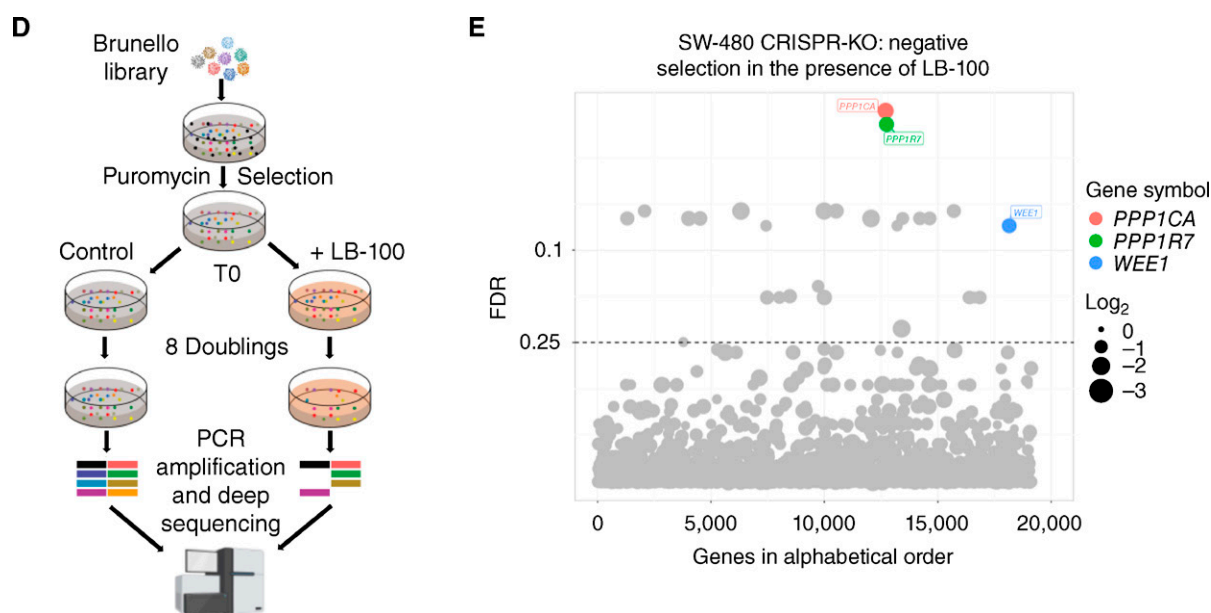
D

Brunello
library

Puromycin ↓ Selection

Control   + LB-100
              T0

8 Doublings

PCR
amplification
and deep
sequencing

E

Figure 2. *(Continued)* **D,** Schematic outline of the CRISPR-KO screen. **E,** The bubble plot shows gRNAs significantly depleted in the LB-100–treated (2.5 μmol/L) arm compared with the untreated controls. Four different gRNAs per gene were tested in 3 replicates. Cells on both conditions were grown for at least 8 population doublings before DNA harvesting and sequencing. Hits were called based on a 0.25 false discovery rate (FDR) and at least 1 log₂ fold-change difference between treated and untreated samples. Only the hits mentioned in the main text are named and colored, the full list of hits is presented in Supplementary Table S7.

mobility shift of 4E-BP1 (indicative of activation by phosphorylation) was noticeable after LB-100 treatment, corroborating mTORC1 activation. Moreover, AXIN2, a transcriptional target of the WNT/β-catenin pathway, was upregulated by LB-100 in HT-29 cells. Similarly, the levels of active β-catenin increased in SW-480 cells, supporting the positive enrichment of the WNT signaling gene set observed in these cell lines. The engagement of stress response pathways was also apparent at the protein level as γ-H2AX and p-CHK1, common markers of DNA damage or replication stress, increased after LB-100 treatment in both cell lines. A sharp increase in p-IRE1α, a major proxy for UPR activation, was also induced by LB-100 in these models. A noticeable increase in the master transcriptional regulator of hypoxia response, HIF1α, was found in SW-480 cells, but not in HT-29. Furthermore, modest PARP cleavage was evident on both colorectal cancer models 24 hours after LB-100 treatment (Fig. 1B). Despite the evident activation of oncogenic signaling pathways induced by LB-100, IncuCyte-based cell proliferation assays showed no increase in cell proliferation induced by 1, 2, or 4 μmol/L of LB-100 in the colorectal cancer panel. Instead, impaired cell proliferation is evident across the panel (Fig. 1C).

We next performed two genome-wide CRISPR screens to identify genes modulating LB-100 toxicity. Using HT-29 cells as a model, we carried out a CRISPRa screen to identify genes whose overexpression increases LB-100 toxicity. This screen identified 53 genes whose overexpression was selectively toxic in the presence of LB-100 (Supplementary Fig. S2A and Supplementary Table S2). Among these genes we find protooncogenes often upregulated in human cancers (i.e., *BCL9L, CCND1, CCNE2, ETS1, MAP3K1, MYC,* and *MYB*), suggesting that increased oncogenic signaling sensitizes cancer cells to LB-100 toxicity. In a complementary CRISPR-knockout (KO) screen in SW-480 cells, we interrogated which gene knockouts could

attenuate LB-100 toxicity. Supplementary Fig. S2B shows that gRNAs targeting genes from the WNT/β-catenin (*CTNNB1, BCL9L,* and *LEF1*) or MAPK (*MAPK14/p38α, MAPK1/ERK2*) signaling pathways were significantly enriched in the samples treated with LB-100 (Supplementary Fig. S2B and Supplementary Table S3). These data indicate that suppression of WNT/β-catenin and MAPK signaling can alleviate the toxicity of LB-100. We combined the hits from both screens and built a String network (18) to infer unbiasedly cellular processes modulating LB-100 toxicity. Indicating only high-confidence interactions, the topology of the network supports the notion that oncogenic signaling modulates LB-100 toxicity (Fig. 1D). Gene Ontology (GO) analyses found that terms associated with β-catenin pathway activity were among the top 3 enriched Biological Processes and Molecular Functions, whereas MAPK activity was the top enriched GO Molecular Function (Fig. 1E). Both the MAPK and β-catenin pathways modulate the transcriptional activity of MYC (19, 20). Using isogenic models (21), we found that higher expression of MYCN, an MYC homolog associated with dismal prognoses in neuroblastoma, increases the sensitivity of neuroblastoma cells to LB-100 (Supplementary Fig. S3A and S3B), validating our findings in an additional cancer model. Together, these data indicate that activation of oncogenic signaling pathways lies at the heart of LB-100 toxicity in colorectal cancer cells. Positive modulation of the WNT/β-catenin and MAPK pathways increased LB-100 toxicity while losing components of these oncogenic pathways alleviated such toxicity.

LB-100 Is Synthetic Lethal with WEE1 Inhibition

We then focused on the notion that increased oncogenic signaling intensifies the dependence on stress response pathways to support cancer cell viability (Fig. 1A and B; ref. 8). This raises the possibility that targeting of stress response pathways might

be synergistic with further activation of oncogenic signaling in killing cancer cells. To investigate this, we designed a custom, stress-focused drug library comprised of 164 selected compounds targeting stress response pathways often associated with malignant phenotypes (i.e., DNA damage stress, oxidative stress, mitotic stress, proteotoxic stress, metabolic stress; Supplementary Table S4). The compounds were selected based on their ability to either induce these stresses or inhibit responses to them. Because senescence can be viewed as a survival response of cells under stress, we also included in the library senolytic drugs, drugs that selectively kill senescent cells (22). Using both HT-29 and SW-480 cells as models, we tested each of these compounds at 15 concentrations, both in the presence and absence of a sublethal dose of LB-100 (2.5 µmol/L; Fig. 2A). The differences in the normalized area under the curve (AUC; with versus without LB-100) for each compound are represented in Fig. 2B; Supplementary Tables S5 and S6. We found that LB-100 increased the toxicity of inhibitors targeting CHK1 and WEE1 in both cell lines (i.e., CHK1 inhibitor GDC-0575 and WEE1 inhibitor adavosertib). Other inhibitors of these kinases were identified in one of two cell lines: CHK1i CCT-245737 and SCH-900776 in HT-29; and CHK1i rabusertib and prexasertib in SW-480. The dual CHK1/WEE1 inhibitor PD0166285 was also identified in SW-480 cells (Fig. 2B). Using GDC-0575 as a CHK1 and adavosertib as a WEE1 inhibitor, we validated that adding LB-100 increases the toxicity of both drugs in these colorectal cancer cells (Fig. 2C). Thus, the stress-focused drug screens identify CHK1 or WEE1 inhibition as a vulnerability of colorectal cancer cells treated with LB-100.

As an unbiased investigation of potential vulnerabilities of cells treated with LB-100, we searched for genes whose knock-out is selectively toxic in the presence of the same sublethal dose of LB-100 (2.5 µmol/L) used in the drug screen (Fig. 2D). This additional arm of the genome-wide CRISPR-KO in SW-480 cells revealed 17 genes whose gRNAs were significantly depleted in the LB-100–treated samples compared with the untreated controls (Fig. 2E; Supplementary Table S7). Among these genes are the catalytic (*PPP1CA*) and one regulatory subunit (*PPP1R7*) of protein phosphatase 1 (PP1), indicating an increased dependence on the activity of this other major Ser/Thr protein phosphatase (23) upon PP2A inhibition. Interestingly, and consistent with the compound screens, gRNAs targeting *WEE1* were also significantly depleted from LB-100—treated samples compared with the untreated controls (Fig. 2E).

Data from the stress-focused drug screens and the genome-wide CRISPR screen converge to identify synthetic lethality between LB-100 and WEE1 inhibition in two colorectal cancer models. CHK1 inhibitors also showed increased toxicity in combination with LB-100 in our drug screens. However, the clinical development of most of these inhibitors has been discontinued (24), discouraging further investigation. We therefore focused subsequent experiments on validating the combination of LB-100 and WEE1 inhibition in a panel of colorectal cancer models and a mechanistic understanding of the combined toxicity. Importantly, the knockdown of the scaffold subunit PPP2R1A also increased the toxicity of WEE1 inhibition in HT-29 and SW-480 cells (Supplementary Fig. S3C and S3D). These data indicate that the sensitization to WEE1 inhibition is not an LB-100–specific phenomenon and results primarily from its effect on PP2A. Accordingly, two structurally unrelated inhibitors of PP2A, calyculin A and okadaic acid, engaged transcriptional programs similar to those observed for LB-100 in these colorectal cancer models (Supplementary Fig. S3E).

LB-100 Is Synergistic with Adavosertib in Multiple Cancer Models

We next used adavosertib as a WEE1 inhibitor to test the effect of the combination with LB-100 in the panel of seven colorectal cancer cell lines. Adavosertib dose-response assays indicated IC_{50} values ranging from around 0.18 to 1 µmol/L across the panel (Supplementary Fig. S4A). We then sought to address the toxicity of the combination in long-term viability assays (see Methods). To that end, we first tested LB-100 and adavosertib as single drugs in this experimental setup and found variable toxicity of both drugs across the panel (Supplementary Fig. S4B), as anticipated by the drug-response assays. Informed by the toxicity of the single drugs, we addressed how sublethal concentrations of each drug would increase toxicity in combination. The results indicate strong toxicity of the combination using concentrations at which the single drugs show, at best, a modest effect (Fig. 3A). It is noteworthy that DLD1, HCT-116, and SW-480 were largely tolerant to up to 500 nmol/L of adavosertib, but such tolerance was abolished in the combination with LB-100 (Fig. 3A). Toxicity of the combination was further confirmed across the colorectal cancer panel by IncuCyte-based cell proliferation assays. Doses of LB-100 or adavosertib that individually have a mild or transient impact ensued a more

Figure 3. The combination of LB-100 and adavosertib is synergistic in cancer cells from different tissues and diverse genetic background. **A,** Long-term viability assays show 7 colorectal cancer (CRC) models treated with LB-100, adavosertib, or the combination at the indicated concentrations. Cultures were refreshed every 2–3 days, and the cells were grown for 10–14 days before fixing, staining, and imaging. **B,** Synergy scores for the combination of LB-100 and adavosertib across 7 colorectal cancer models. Cells were treated with 5 concentrations of LB-100 (1, 2, 3, 4, and 5 µmol/L) or adavosertib (100, 200, 300, 400, and 500 nmol/L) and all respective permutations for 4 days. The percentage of cell viability for each condition was estimated by resazurin fluorescence and normalized to DMSO controls. Synergyfinder.org web tool was used to calculate the ZIP synergy scores. Three independent experiments are represented. **C** and **D,** Long-term viability assays for 4 PDAC and 4 CCA models, respectively, treated with LB-100, adavosertib, or the combination at the indicated concentrations. Cultures were refreshed every 2–3 days, and the cells were grown for 10–14 days before fixing, staining, and imaging. **E** and **F,** Synergy scores for the combination of LB-100 and adavosertib across 4 PDAC and 4 CCA models, respectively. Cells were treated with 5 concentrations of LB-100 (1, 2, 3, 4, and 5 µmol/L) or adavosertib (100, 200, 300, 400, and 500 nmol/L) and all respective permutations for 4 days. The percentage of cell viability for each condition was estimated by resazurin fluorescence and normalized by DMSO controls. Synergyfinder.org web tool was used to calculate the ZIP synergy scores. Three independent experiments are represented. **G,** Synergy scores for the indicated combinations of LB-100, adavosertib, doxorubicin, and gemcitabine across 6 cancer cell models. Cells were treated for 4 days with 10 concentrations of each drug: LB-100 (0.5, 1, 2, 3, 4, 5, 6, 7, 8, and 9 µmol/L); adavosertib (50, 100, 200, 300, 400, 500, 600, 700. 800, 900 nmol/L); doxorubicin (5, 10, 20, 30, 40,50, 60, 70, 80, and 90 nmol/L); gemcitabine (0.63, 1.25, 2.5, 5, 10, 20, 30, 40, 50, and 60 nmol/L); and all respective permutations for the combinations tested. The percentage of cell viability for each condition was estimated by resazurin fluorescence and normalized by DMSO controls. Synergyfinder.org web tool was used to calculate the ZIP synergy scores. Three independent experiments are represented.
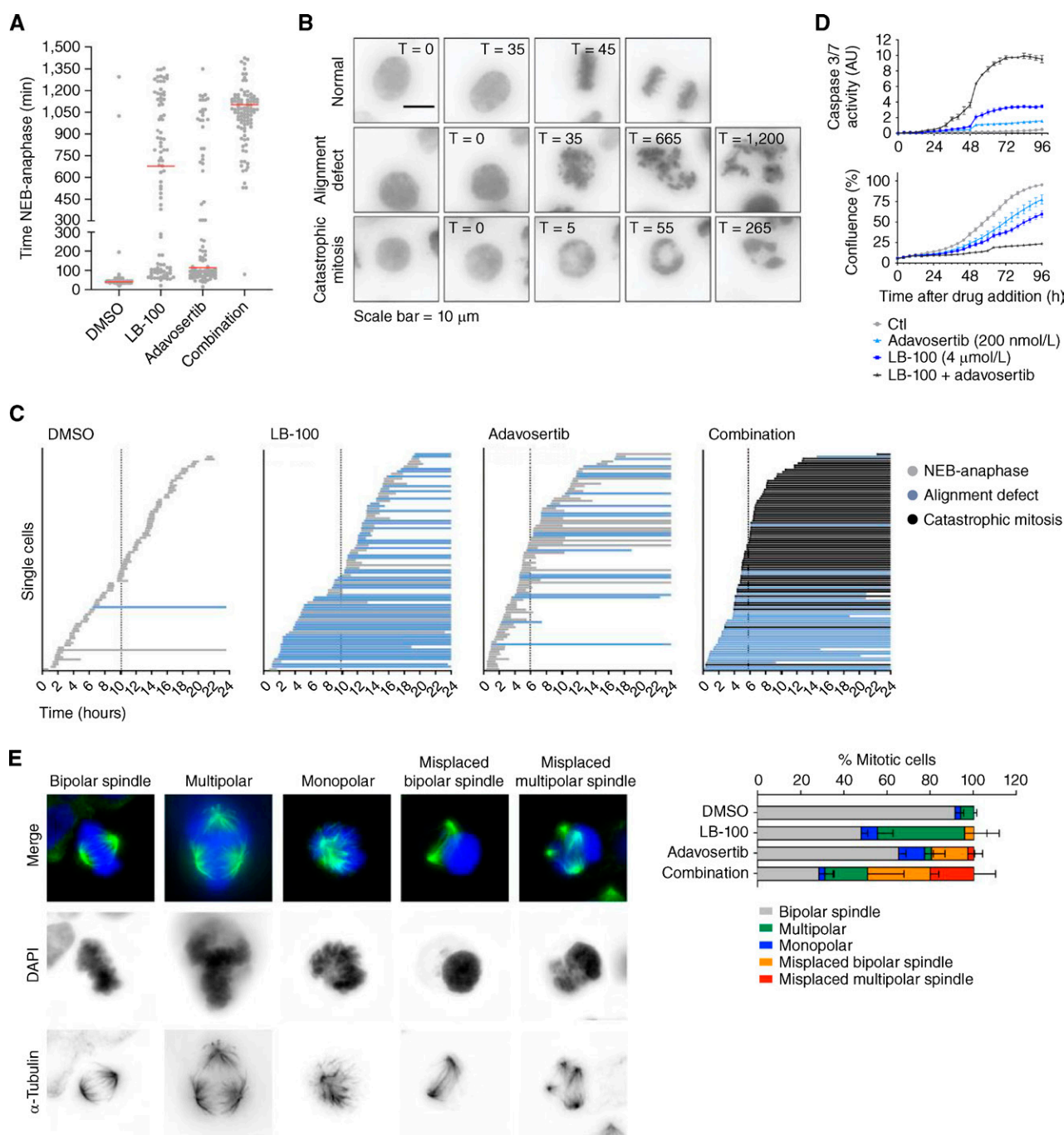
American Association for Cancer Research®
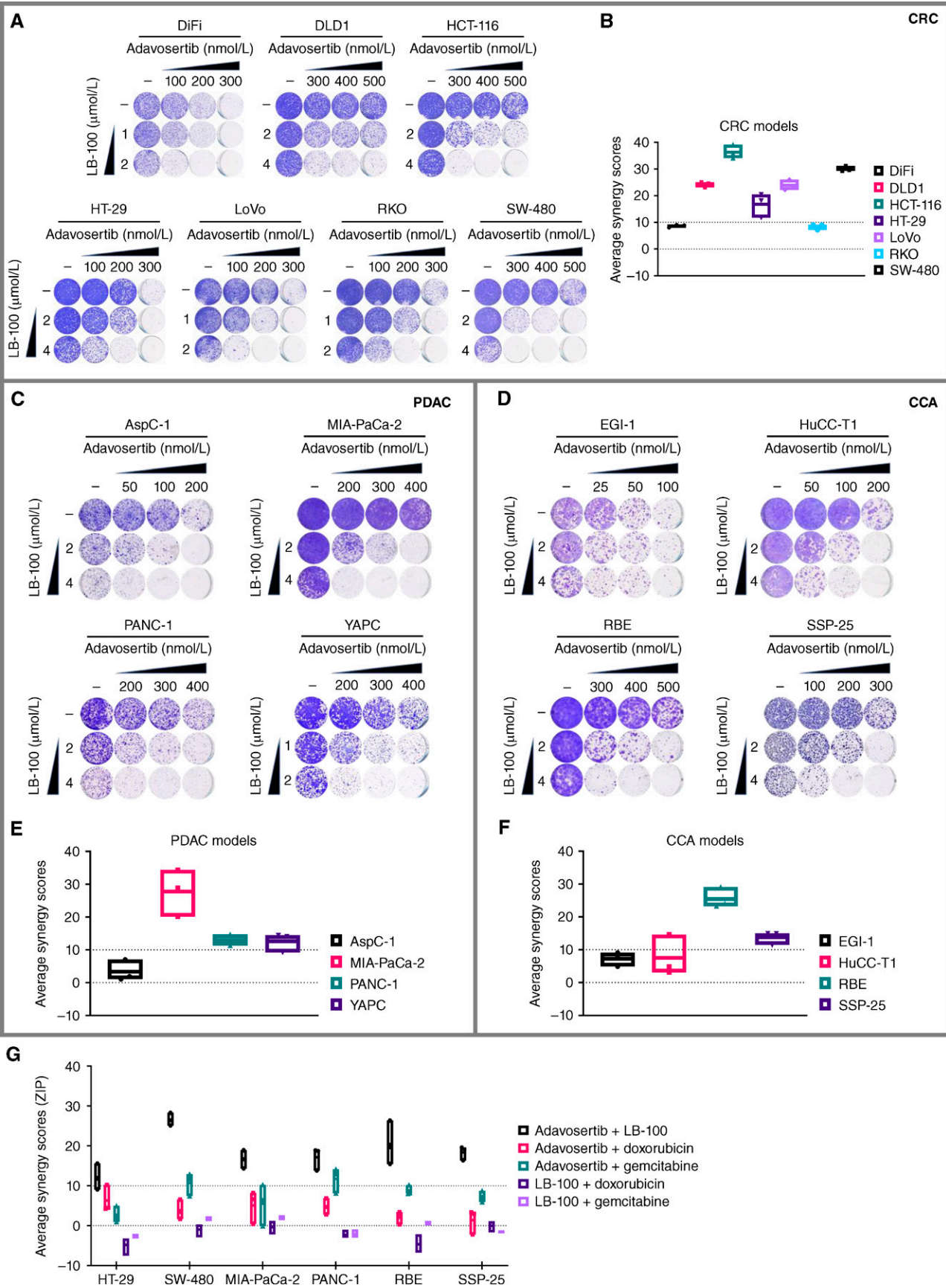
Figure 4. The LB-100 and adavosertib combination leads to aberrant mitoses and cell death. **A,** Time from nuclear envelope breakdown (NEB) to anaphase for HT-29 cells untreated (DMSO) or treated with LB-100, adavosertib, or the combination. Each dot represents an individual cell followed by live-cell imaging. Red bars represent the average time spent from NEB to anaphase. Two independent experiments are compiled ($n = 100$ cells per condition). **B,** Representative live-cell microscopy images of HT-29 cells. The examples highlight the two major mitotic phenotypes observed. The scalebar represents 10 μm. **C,** Representation of the time for mitotic entry and exit of HT-29 cells imaged every 5 minutes for 24 hours, starting immediately after the addition of DMSO, LB-100, adavosertib, or the combination. Each bar represents an individual cell. The colors of the bars indicate normal or aberrant mitoses. The beginning of the bars marks NEB and the end represents either anaphase or end of the experiment. Dashed vertical lines represent the average times for mitotic entry after the addition of the drugs. **D,** IncuCyte-based assay for caspase-3/7 activity. Cells were treated with DMSO, LB-100, adavosertib, or the combination in the presence of a caspase-3/7 apoptosis assay reagent. Green fluorescence from the apoptosis assay reagent divided by the total confluence was used to estimate apoptosis for 96 hours. **E,** Representative images (left) and quantification (right) of spindle defects in mitotic cells treated with DMSO, LB-100, adavosertib, or the combination. Cells were treated for 8 hours before fixation. DNA was stained with DAPI (blue) and α-Tubulin was immunostained (green). Quantification is based on 2 independent experiments each analyzing 50 cells per condition. (*continued on next page*)
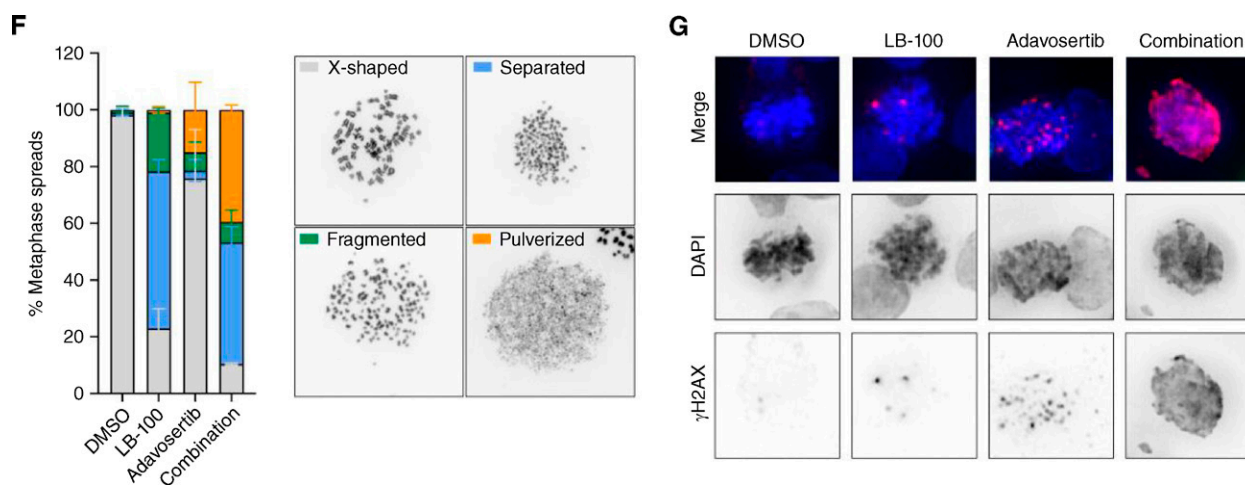
Figure 4. *(Continued)* **F,** Chromosome spreads from HT-29 cells treated with DMSO, LB-100, adavosertib, or the combination. On the left, quantification of chromosome integrity; on the right, are representative images. Drugs were added for 16 hours and then nocodazole was added for an additional hours to block cells in mitosis. Cells were harvested by mitotic shake-off for spreading. **G,** Representative images show HT-29 cells treated with DMSO, LB-100, adavosertib, or the combination for 24 hours. After fixation, total DNA was stained with DAPI (blue) and γ-H2AX was immunostained (red). Throughout the figure, LB-100 was used at 4 µmol/L and adavosertib at 200 nmol/L.

sustained restraint of cell proliferation in combination (Supplementary Fig. S4C). Next, we expanded the range of doses tested, to address if the two drugs act synergistically in these colorectal cancer cells. Synergy matrices combining 5 doses of each drug showed toxicities larger than expected based on the effect of the single drugs, as indicated by the respective synergy scores in five out of seven cell lines (Fig. 3B), whereas DiFi and RKO cells showed synergy scores slightly below the proposed threshold of 10 for synergy (25). These results confirm the combined toxicity of LB-100 and adavosertib in a diverse set of colorectal cancer cell lines, indicating no critical dependence on a specific set of oncogenic driver mutations in colorectal cancer. It is noteworthy that BJ fibroblasts and HaCaT keratinocytes, two nonmalignant human cell models, were less sensitive to LB-100 compared with average sensitivity across the colorectal cancer models tested (Supplementary Fig. S4D). BJ cells were also less sensitive to adavosertib, whereas the sensitivity of HaCaT cells was comparable with the average of the colorectal cancer panel. Importantly, at the same doses used on the colorectal cancer cell panel, we found no synergy between the two drugs in BJ or HaCaT cells (Supplementary Fig. S4E).

The efficacy of the combination in the colorectal cancer models encouraged us to test it in other tumor types lacking effective treatment options. Pancreatic ductal adenocarcinomas (PDAC) are refractory to conventional therapies, and the 5-year survival rates remain one of the lowest among all cancers (26). Similarly, despite a much lower overall incidence, cholangiocarcinomas (CCA) share with PDACs the frequent lack of response to conventional therapies and the dismal prognosis (27). We put together a small panel of four PDAC cell lines, and a similar one of CCA cells (Supplementary Table S1) to assess the potential of the combination of LB-100 and adavosertib in these cancer types. LB-100 dose-response assays revealed IC$_{50}$ values varying from 3.2 to >10 µmol/L in the PDAC cells (Supplementary Fig. S5A), and from 4.7 to >12 µmol/L in the CCA models

(Supplementary Fig. S5B). For adavosertib, the IC$_{50}$ values ranged from 0.3 to 1.7 µmol/L in the PDAC models (Supplementary Fig. S5A), and from 0.1 to 0.37 µmol/L in the CCA models (Supplementary Fig. S5B). To test the effects of the combination in the PDAC and CCA cancer models systematically, we used the same experimental workflow used for the colorectal cancer panel. We first addressed the long-term toxicity of LB-100 and adavosertib in the PDAC and CAA models (Fig. S5C and S5D). Then, we combined sublethal doses of each drug and found strong or complete suppression of cell viability in the models from both cancer types (Fig. 3C and D). Cell proliferation assays corroborate that doses of the individual drugs that are ineffective in the suppression of cell proliferation in each of the PDAC and CCA models become quite effective when used in combination (Supplementary Fig. S5E and S5F). Furthermore, matrices combining LB-100 and adavosertib indicated synergy in 3 out of the 4 PDAC models (Fig. 3E). For the CCA panel, we found synergy scores above the threshold for RBE and SSP-25, but not for EGI and HuCC-T1 cells (Fig. 3F).

Preclinical data support the efficacy of adavosertib in combination with chemotherapy, which has subsequently been investigated in multiple clinical trials (28). Likewise, LB-100 has been proposed as a sensitizer for chemotherapy (14) and is currently under clinical investigation in such combination (NCT04560972). We asked how the combination of LB-100 and adavosertib compares with each of these drugs in combination with doxorubicin or gemcitabine. We performed synergy matrices using 10 concentrations of each drug in 2 cell models per tumor type. The results showed higher synergy scores for the combination LB-100 + adavosertib compared with combinations with the chemotherapeutic agents in each of the models (Fig. 3G).

These data reveal considerable context independence of the synthetic lethality between LB-100 and adavosertib in cancer cell lines from different tissues and diverse genetic
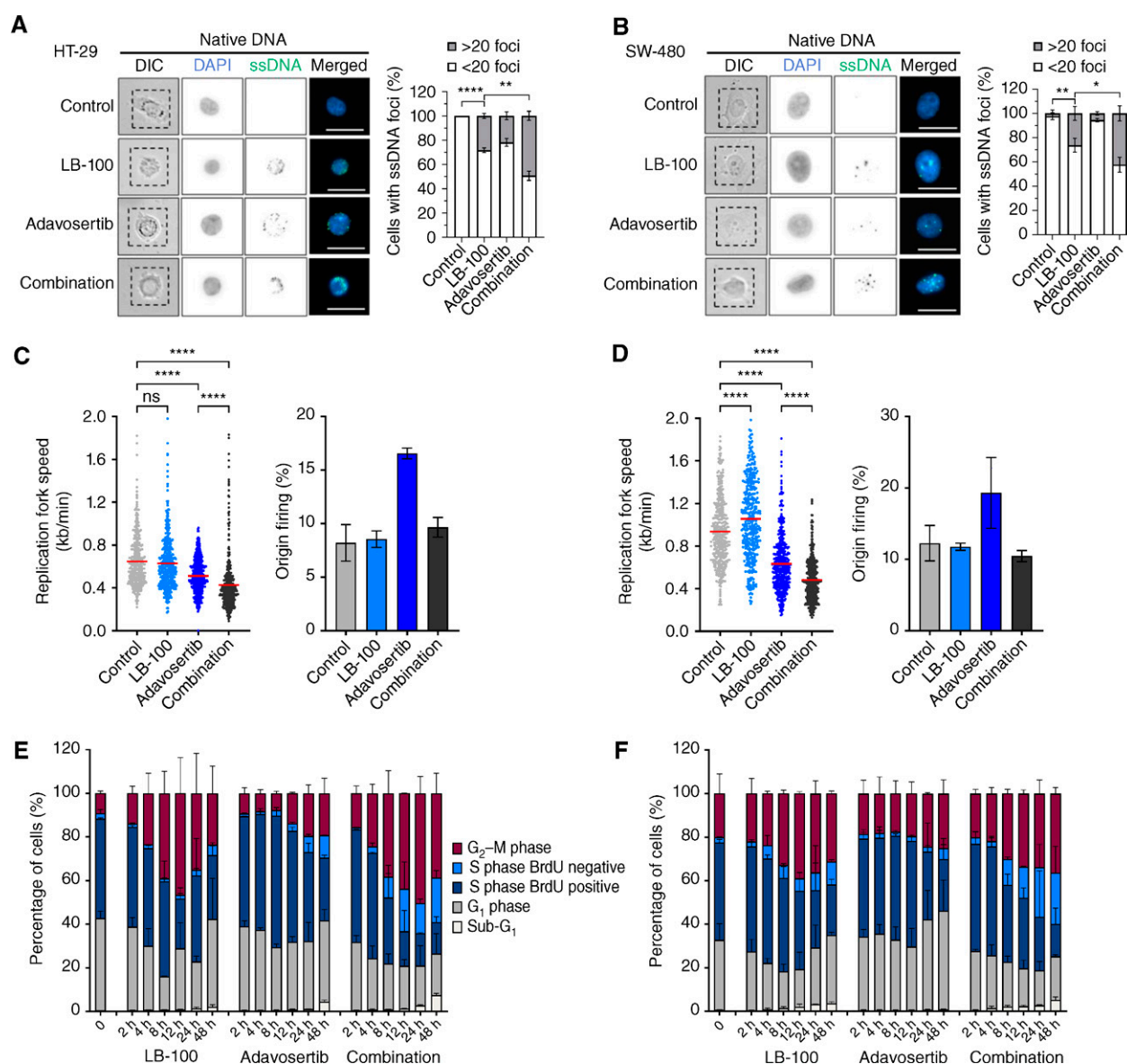
Figure 5. LB-100 and adavosertib promote concerted replication stress, priming for premature mitoses. Representative images and quantifications of single-strand DNA ssDNA foci in HT-29 (**A**) and SW-480 (**B**) cells. After incorporating BrdUrd for 48 hours, the cells were treated as indicated for 8 hours and then fixed. Total DNA was stained with DAPI (blue) and BrdUrd was immunostained (green) under non-denaturing conditions to indicate long fragments of ssDNA. Quantification is based on 2 independent experiments analyzing at least 100 cells per coverslip. Asterisks indicate significance level (*, $P < 0.05$; **, $P < 0.01$; ****, $P < 0.0001$) by two-tailed unpaired t test. **C** and **D**, DNA fiber assays show replication fork speed (left) and percentage of origin firing (right) of HT-29 and SW-480 cells, respectively, untreated (DMSO) or treated with LB-100, adavosertib, or the combination for 8 hours. For fork speed, track lengths of at least 380 ongoing forks from each condition were measured with ImageJ in 2 independent experiments that are shown combined. Red lines indicate the mean and asterisks indicate the significance level (****, $P < 0.0001$) by the nonparametric Kruskal–Wallis test. For origin firing, first-label and second-label origins are shown as a percentage of all labeled tracks. At least 1,000 labeled tracks per condition were analyzed. **E** and **F,** Quantification of time-course cell-cycle flow cytometry from HT-29 and SW-480 cells, respectively, treated with LB-100, adavosertib, or the combination. Cells were fixed at the indicated time points after the addition of the drugs. BrdUrd (10 µmol/L) was added 1 hour before fixation. Total DNA was stained by propidium iodide (PI) and BrdUrd was immunostained. Cell-cycle phases were gated using the FlowJo software. Error bars represent the standard deviation of 2 independent experiments. (*continued on next page*)

backgrounds. Moreover, they suggest that the combination proposed here might provide therapeutic benefits superior to regimens that are currently under clinical investigation. We, therefore, focused next on the mechanistic understanding of the toxicity and evaluating the viability of this combination *in vivo*.

The Combination LB-100 and Adavosertib Leads to Aberrant Mitoses and Cell Death

WEE1 inhibition abrogates the G_2–M cell-cycle checkpoint, allowing cells to enter mitosis without resolving DNA damage, leading to mitotic catastrophe and apoptosis (29). Similarly, LB-100 has been shown to induce mitotic catastrophe
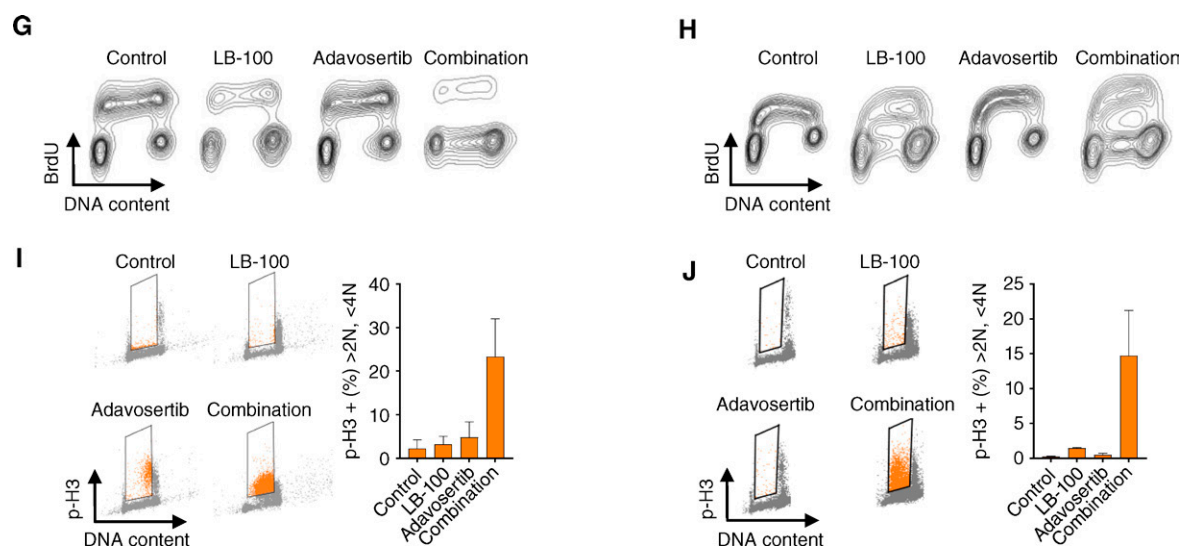
Figure 5. *(Continued)* **G** and **H,** Representative image of the 12-hour time point from the time-course flow cytometry above. **I** and **J,** Flow cytometry assessment of p-H3 (Ser10) vs. DNA content in HT-29 and SW-480 cells, respectively, treated with LB-100, adavosertib, or the combination for 12 hours. Total DNA was stained by propidium iodide (PI) and p-H3 (Ser10) was immunostained. S-phase cells were gated using the FlowJo software. Error bars represent the standard deviation of 2 independent experiments. Throughout the figure, LB-100 was used at 4 μmol/L on both cell lines. Adavosertib was used at 200 nmol/L in HT-29 and 400 nmol/L in SW-480.

in several tumor models, particularly in combination with DNA-damaging agents (15). It is well established that the unscheduled proliferation inherent to cancer cells comes at the expense of abnormal mitoses and associated mitotic stress (30). This raises the question of whether the observed synergy of these drugs results from fatal mitotic defects.

To address this, we followed HT-29 cells expressing H2B-GFP by live-cell imaging from nuclear envelope breakdown (marking mitotic entry) until anaphase onset. Numerous positive feedback loops ensure complete commitment to mitosis upon mitotic entry (31), and such an "all-in" process takes place in a fraction of the cell-cycle time. Accordingly, we found that DMSO-treated cells spent an average of 50 minutes in mitosis. LB-100–treated cells, however, spent on average over 600 minutes in mitosis, with prominent variability among individual cells. Adavosertib also increased the average time spent in mitosis, although to a lesser extent (~100 minutes). The combination resulted in an average time in mitosis of over 1,050 minutes with virtually all cells showing markedly long mitoses (Fig. 4A). Detailed analyses of the time-lapse images revealed defective chromosome alignment and highly catastrophic mitoses as the two major phenotypes induced by these drugs (Fig. 4B). Defective chromosome alignment was highly prevalent in the LB-100–treated cells in the first hours after the addition of the drug, and alleviated in cells entering mitosis later (Fig. 4C, second panel). Adavosertib induced fewer but similar misalignments in cells entering mitosis later and sharply reduced the average time for mitotic entry to less than 6 hours, compared with about 10 hours in the control-and LB-100–treated cells (Fig. 4C, third panel). Cells treated with the combination showed both the accelerated mitotic entry observed for adavosertib and the high prevalence of misalignments shortly after drug exposure observed for LB-100. Strikingly, most of the combination-treated cells entering mitosis later showed catastrophic mitoses with only

partial chromatin condensation and failed attempts to divide until the end of the experiment (Fig. 4C, fourth panel). This phenotype was not observed in the cells treated with the single drugs. These results reveal that the combination therapy in HT-29 colorectal cancer cells results in a defective mitotic-like state that persists for at least 24 hours following drug exposure. Although the time-lapse experiments did not indicate the fate of these cells, measurements of caspase-3/7 activity for 96 hours show apoptosis induction in the cells treated with the combination (Fig. 4D).

To better understand the observed mitotic defects, we next examined the microtubule organization of mitotic cells in response to the single drugs and the combination. The vast majority of the DMSO-treated cells showed the expected bipolar spindles attached to the metaphase plate. LB-100 treatment induced multipolar spindles in about 40% of the mitotic cells, whereas adavosertib increased the frequency of monopolar and misplaced bipolar spindles. Aberrant spindles were found in over 70% of the cells treated with the combination of these drugs (Fig. 4E). The abnormalities observed in these mitoses also included multipolar and misplaced bipolar spindles. However, misplaced multipolar spindles were only frequent in combination-treated cells, further indicating mitotic defects emerging from the combination.

As an additional readout for mitotic defects, we addressed chromosome integrity across the different treatments. Chromosome spreads from DMSO-treated cells showed the expected paired chromatids attached at the primary constriction (Fig. 4F). LB-100 treatment largely increased the frequency of separated and fragmented chromatids, which is consistent with the misalignment phenotype observed in Fig. 4C. Adavosertib treatment compromised chromosome integrity in nearly 30% of the cells, with a fraction of them failing to produce discrete chromosomes. Such "pulverized"
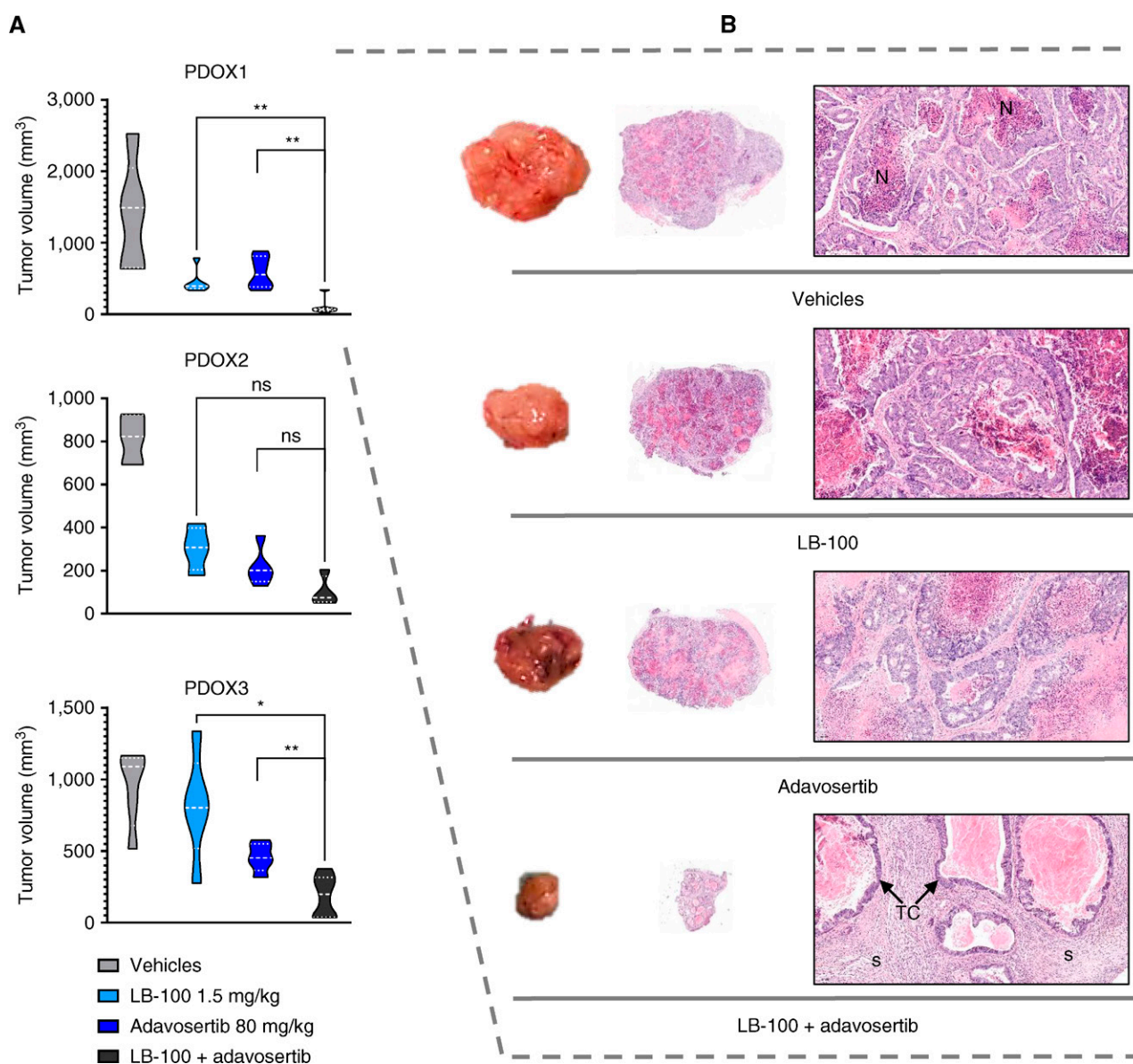
Figure 6. The LB-100 and adavosertib combination restrains tumor growth *in vivo*. **A,** Endpoint tumor volumes of 3 independent orthotopic colorectal cancer PDXs treated with LB-100, adavosertib, or the combination for 4 weeks. After transplantation and engraftment, the mice were randomized and treated as indicated. LB-100 was given on days 1, 3, and 5, whereas adavosertib was administered on days 1–5 in 7-day cycles. Asterisks indicate significance level (*, $P < 0.05$; **, $P < 0.01$) by two-tailed Mann–Whitney test. **B,** Representative tumors and hematoxylin and eosin stainings at endpoint from PDOX1 treated as indicated. Original magnification middle images: 15×, scale bar, 1,000 μm; right images: 200×. N indicates necrotic areas, S indicates stroma, and the arrows point to the tumor-cell component. (*continued on next page*)

spreads were present in about 40% of the cells exposed to the combination, and separated chromatids, as observed for LB-100 single treatment, were also frequent (Fig. 4F). These observations align with the misplaced spindles shown in Fig. 4E, given that those pulverized chromosomes could not establish a proper metaphase plate. Such an apparent chromosome fragmentation also indicates severe DNA damage in these mitotic cells. In line with that, imaging of mitotic HT-29 cells treated with the combination revealed a pannuclear γ-H2AX staining instead of punctate foci observed in LB-100– or adavosertib-treated γ-H2AX–positive cells (Fig. 4G). Altogether, these data indicate that the combined induction

of catastrophic mitoses followed by cell death underlies the synergy between LB-100 and WEE1 inhibition in colorectal cancer cells.

LB-100 and Adavosertib Cause Concerted DNA Replication Stress, Priming Cancer Cells to Premature and Deadly Mitoses

It has been shown previously that WEE1 inhibition not only abrogates the G_2–M checkpoint but can also drive S-phase cells under replication stress into premature mitoses (32). Such a scenario would be in line with the aberrant mitoses with pannuclear DNA damage described above.
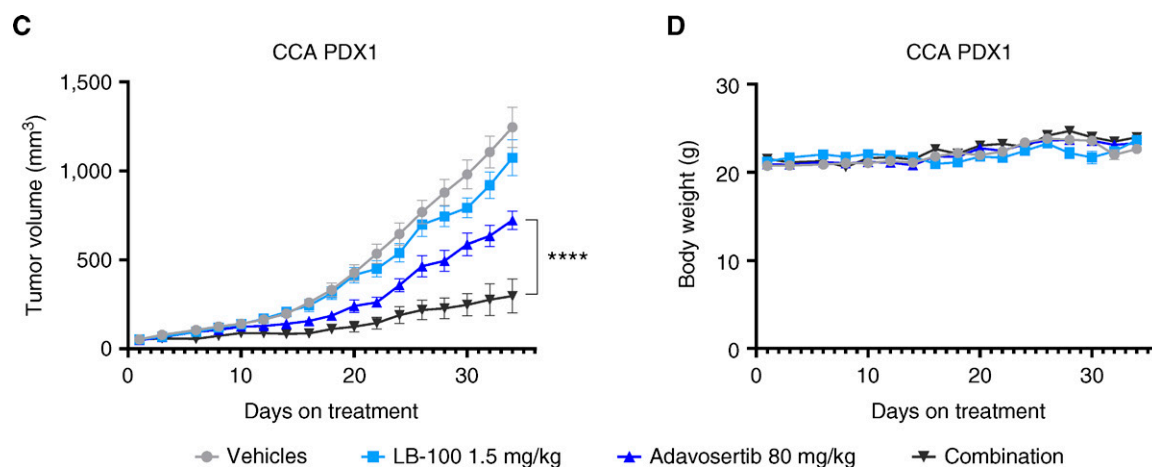
Figure 6. *(Continued)* **C,** Tumor growth curves of cholangiocarcinoma PDX1 treated with LB-100, adavosertib, or the combination. After transplantation and engraftment, the mice were randomized and treated as indicated. LB-100 was given on day 1, adavosertib was given on days 1–3, in 4-day cycles. Tumors were measured 3 times per week. Graphs, mean and SEM. Asterisks indicate significance level (****, $P<0.0001$) by two-way ANOVA with Tukey multiple comparisons. **D,** Body weight variation of the CCA PDX1 across the experiment. Graphs, mean and SEM; PDOX, patient-derived orthotopic xenograft.

We therefore asked whether and how replication stress contributes to the toxicity of the combination. The presence of single-strand DNA (ssDNA) resulting from uncoupled DNA helicase and polymerase activities is direct evidence of replication stress (33). We used BrdUrd detection under native (nondenaturing) conditions as an indication of replication stress. We found that both LB-100 and adavosertib increased the percentage of HT-29 cells with multiple ssDNA foci 8 hours after drug exposure (Fig. 5A). Even more prominent replication stress was present under the combined treatment, with around 50% of the cells showing multiple ssDNA foci (Fig. 5A). Similar results were observed in SW-480 cells; however, adavosertib led only to a mild increase in ssDNA foci in this model (Fig. 5B). We next performed DNA fiber assays on both colorectal cancer models to address the impact of these drugs on the dynamics of DNA replication. LB-100 had no significant effect on the average DNA replication fork speed in HT-29 and modestly increased it in SW-480 cells compared with untreated samples (Fig. 5C and D). The percentage of replication origin firing in both cell models was similar to the respective controls. Adavosertib, however, led to a reduced average fork speed, as previously described (34, 35), and a concomitant increase in the percentage of origin firing in both colorectal cancer models (Fig. 5C and D). An inverse correlation between fork speed and origin firing is characteristic of DNA replication under perturbations (36). This is accomplished by the usage of backup replication origins under stress, given that these origins are licensed in large excess relative to the amount necessary to complete an unperturbed S phase (37, 38). It is therefore noteworthy that the concomitant addition of LB-100 further reduced the slower fork speed observed for adavosertib, but without the concurrent increase in origin firing (Fig. 5C and D). Such a "decoupling" of the inverse correlation between fork speed and origin firing indicates complementary effects of these drugs to disrupt the dynamics of DNA replication forks in these colorectal cancer cells.

Next, we addressed how such a concerted action on replication forks impacts the cell-cycle progression of these colorectal cancer cells. For that, we performed time-course flow cytometry analyses assessing total DNA content and BrdUrd incorporation as a proxy for active DNA synthesis. The results for both HT-29 (Fig. 5E) and SW-480 models (Fig. 5F) show a transient accumulation of cells in G_2–M induced by LB-100, peaking around 12 hours after stimulation. More sustained G_2–M accumulation was observed in the combination-treated samples, whereas adavosertib mildly increased the G_2–M fraction (Fig. 5E and F). Strikingly, in both colorectal cancer models, the samples treated with the combination showed an increased accumulation of cells with S-phase DNA content that are negative for BrdUrd, indicating a lack of active DNA synthesis (Fig. 5E–H). These data confirm that the combination of LB-100 and adavosertib halts DNA replication, as indicated by the fiber assays. In fact, DNA replication is incompatible with a mitotic state, and stalled replication forks are actively cleaved in mitosis (39). The lack of active replication and the pulverized chromosome spreads support a scenario in which the combination of LB-100 and adavosertib drives these colorectal cancer cells to mitosis before completing DNA replication. Corroborating this rationale, in both colorectal cancer models, cells with DNA content between G_1 and G_2–M (compatible with S phase) become positive for the mitosis marker phospho-histone H3 (p-H3; Ser10) 12 hours after treatment with the combination (Fig. 5I and J). Together, the data above indicate that the combination of LB-100 and adavosertib results in severe replication stress, priming these colorectal cancer cells to catastrophic mitoses prior to DNA replication completion.

LB-100 and Adavosertib Combination Restrains Tumor Growth *In Vivo*

The data above show the efficacy of the LB-100 and adavosertib combination in multiple cancer models and how these compounds cooperate to disrupt cancer cell viability.

Although the observed synergistic activity and context independence *in vitro* are promising, the balance between efficacy and toxicity must be tested *in vivo* to indicate a potential therapeutic window. We implanted tumor samples derived from three different colorectal cancer patients in the colon of immunodeficient mice to ask whether the combination of LB-100 and adavosertib suppresses tumor growth *in situ*. It is noteworthy that these orthotopic patient-derived xenografts (PDX) derive from metastatic colorectal tumors with diverse mutation backgrounds that progressed under previous treatment regimens (see Methods). After mice randomization, we treated these PDXs with the single drugs and the combination for four weeks and measured endpoint tumor sizes at sacrifice. The results showed antitumor activity of LB-100 in two of the three PDXs, whereas adavosertib restrained tumor growth in all three PDXs. Yet, in combination, these drugs strongly suppressed tumor growth, showing antitumor activity significantly superior to the single drugs in 2 of the 3 PDXs (Fig. 6A).

In addition to the reduction of tumor size, histopathologic features of tumor regression indicate treatment efficacy and predict patients' prognoses (40). We therefore addressed the endpoint histology of these patient-derived tumors under the four treatment regimens. As highlighted in Fig. 6B, vehicle-treated PDOX1 tumors showed moderately differentiated adenocarcinoma, consisting of closely packed glands with "dirty" luminal necrosis. No obvious histopathologic regression was observed in the tumors treated with LB-100 or adavosertib. However, clear histopathologic regression was found in tumors treated with the combination, showing reduced tumor-cell component, and increased fibrosis and inflammatory infiltrate (Fig. 6B). The moderately differentiated adenocarcinoma PDOX2 showed similar histologic regression for the combination and single drugs (Supplementary Fig. S6A, left). The histology of the poorly differentiated adenocarcinoma PDOX3 tumors was in line with the observed for PDOX1, with similar histopathologic responses for the combination and no obvious effect of the single drugs (Supplementary Fig. S6A, right). The body weight curves indicate that the single drugs and the combination were well-tolerated in these mouse models (Supplementary Fig. S6B). However, 1 of 15 mice treated with LB-100 and 2 of 22 treated with the combination died during the experiment. These casualties cannot be unequivocally attributed to treatment toxicity ($P > 0.45$). Moreover, we dosed LB-100 at 1.5 mg/kg; this drug has been extensively tested in multiple mice models in doses ranging from 1.5 to 2.5 mg/kg without noticeable toxicity, even in combination with chemotherapy (14).

Nevertheless, to address further the potential toxicity of the combination over normal tissues, we analyzed the heart, liver, lung, and spleen from PDOX1 and PDOX2 mice. No treatment-related alterations were found in these mice (Supplementary Fig. S7).

Expanding our analyses to a different tumor type, we transplanted patient-derived cholangiocarcinoma tumor fragments into the flank of immunocompromised mice. After engraftment and randomization, we treated these mice with LB-100, adavosertib, or the combination until the vehicle-treated control group reached the endpoint. In this PDX, LB-100 alone showed little antitumor effect, whereas adavosertib delayed tumor growth more obviously. Yet, the combination promoted an antitumor effect clearly superior to any of the single drugs and strongly restrained tumor growth in this CCA PDX (Fig. 6C). It is noteworthy that no casualties were observed in any treatment groups throughout the experiments and the body weight curves indicate that the combination was tolerated by the mice (Fig. 6D). These results confirm the antitumor activity of the combination LB-100 + adavosertib in patient-derived models using doses not associated with systemic toxicity.

Acquired Resistance to the Combination of LB-100 and Adavosertib Is Tumor-Suppressive

Even highly synergistic drug combinations can ultimately result in resistance in patients with advanced disease (41). Because deliberate further activation of oncogenic signaling fundamentally differs from inhibition of these signals, we studied how cancer cells may acquire resistance to the combination of LB-100 and adavosertib. We selected polyclonal pools of HT-29– and SW-480–resistant cells (HT-29-R and SW-480-R) by culturing parental cells in the presence of the drug combination for over four months. Long-term viability assays illustrate the reduced toxicity of the combination in the resistant cells compared with the respective parental cells (Fig. 7A). IncuCyte-based proliferation assays showed that both combination-resistant models proliferate slower than their respective parental cells (Supplementary Fig. S8A). Moreover, despite growing in the presence of the drugs for several months, there is no apparent "addiction" to the combination. Instead, for HT-29 combination-resistant cells, the combination still hinders cell proliferation (Supplementary Fig. S8A, left).

We reasoned that acquired resistance to hyperactivation of oncogenic pathways might lead to the downmodulation of oncogenic signaling to evade the stress imposed by the increased signaling. Indeed, JUN is no longer hyperactivated

Figure 7. Acquired resistance to the combination of LB-100 and adavosertib is tumor-suppressive. **A,** Long-term viability assays show HT-29 and SW-480 parental and resistant cells treated with LB-100, adavosertib, or the combination at the indicated concentrations. Cultures were refreshed every 2–3 days, and the cells were grown for 10–14 days before fixing, staining, and imaging. **B,** Western blots show selected oncogenic signaling and stress response pathways in HT-29 and SW-480 parental and resistant cells. Parental cells were exposed to the combination for 24 hours, whereas for resistant cells, that grow in the presence of the combination, the drugs were washed out (w/o) 24 hours before harvesting. LB-100 was used at 4 μmol/L and adavosertib was used at 400 nmol/L. Vinculin was used as a loading control. **C,** UMAP representations of HT-29 (top) and SW-480 (bottom) parental and resistant cells colored by a sample of origin (left) or by clusters (right). Parental cells were harvested untreated and resistant cells were harvested 24 hours after the washout of the drugs. **D,** Tumor growth curves of SW-480 parental and resistant cells in the absence of drugs. Per cell line, 10 mice were injected subcutaneously with 3 million cells and we measured tumor size 3 times per week. Graph, mean and SEM of the measurements until the first mouse reached 1,500 mm³ (ethical sacrifice). **E,** Kaplan–Meier survival curves of the experiment above along 3 months considering the 1,500 mm³ ethical sacrifice.
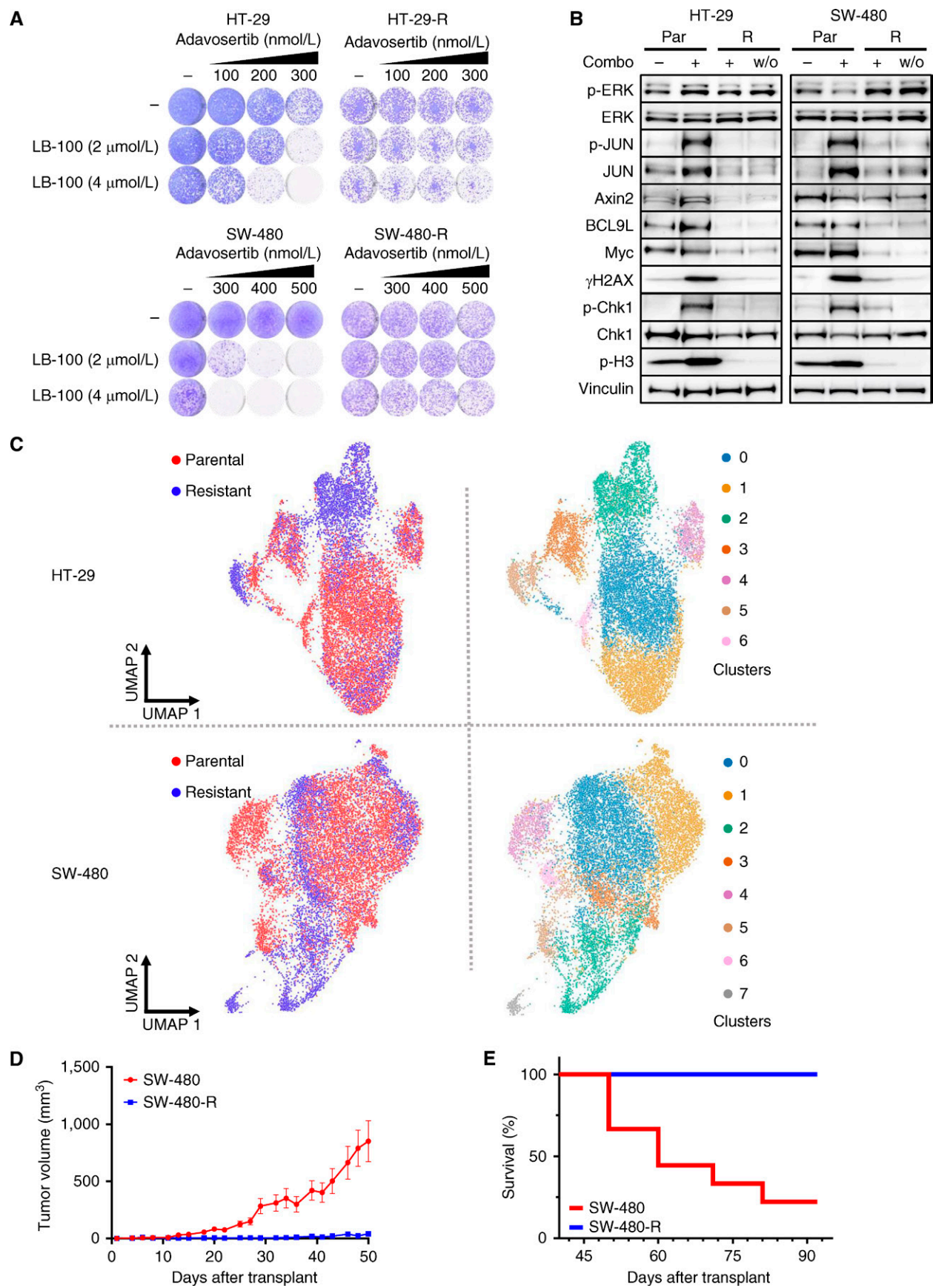
in the resistant cells in the presence of drugs, suggesting a downmodulation of this MAPK signaling arm. Furthermore, the levels of the β-catenin targets AXIN2 and MYC and the modulator of β-catenin transcriptional activity BCL9 L were lower in the resistant cells, even in the absence of the drugs (Fig. 7B). In contrast, p-ERK levels remained higher in the combination-resistant cells compared with parental controls. For both colorectal cancer models, p-CHK1, γ-H2AX, and p-H3 (Ser10) levels are also no longer increased in the presence of the drug (Fig. 7B). These data indicate downmodulated β-catenin and JUN signaling coincident with alleviated replication and mitotic stresses after acquired resistance to LB-100 + adavosertib in these colorectal cancer cells.

Our data show the presence of numerous mitotic defects induced by the combination of LB-100 and adavosertib in these colorectal cancer cells (Fig. 4). HT-29 and SW-480 karyotypes have been described as near triploid (42), illustrating the aneuploidy characteristic of cancer cells. We asked whether acquired resistance to that combination affected the aneuploidy in these colorectal cancer models. To address this, we prepared chromosome spreads from the parental and combination-resistant cells and counted the number of chromosomes. The results showed that HT-29-R cells have a median chromosome number of 62, compared with about 66 on HT-29 parental cells (Supplementary Fig. S8B, left). SW-480 parental cells showed marked heterogeneity in the number of chromosomes across the population, with a median number of 80. Such heterogeneity was sharply reduced in the SW-480-R cells that showed a median of 54 chromosomes (Supplementary Fig. S8B, right). These data evidence reductions of aneuploidy during the acquired resistance to the combination of LB-100 and adavosertib in these colorectal cancer cells.

To gain a deeper understanding of the nature of the resistance and the heterogeneity of these polyclonal populations, we performed single-cell RNA sequencing (RNA-seq) on HT-29-R and SW-480-R and their respective parental cells. We analyzed over 4,000 cells per model, which yielded 7 UMAP clusters for HT-29 and 8 for SW-480 cells after processing and integration, performed independently per cell line (see Methods). Interestingly, for HT-29, we can observe that cluster 2 is virtually absent in parental cells, whereas they compose most of the clusters 0 and 1 (Fig. 7C, top). For SW-480 cells, whereas clusters 2 and 7 are populated mostly by resistant cells, the major clusters 0 and 1 show a mix of parental and resistant cells (Fig. 7C, bottom). By analyzing the marker genes making the identity of each cluster, we observe that, for HT-29 cells, clusters 0 and 1 are defined by several genes associated with proliferation (e.g., *MCM3/4/6*, *CDC6*, *PLK1*, *AURKA*, *CCNB1/2*, *CCNA2*, *MKI67*, among others). The resistance-associated cluster 2 shows a rather low expression of most of these genes and displays marker genes associated with inflammation (Supplementary Fig. S8C, left). In SW-480 cells, although the specific genes vary, similar inflammation-related markers were observed for cluster 2, which is also composed of combination-resistant cells. In this model, only a few markers discriminate cluster 0 from the other cells. Cluster 1, however, showed expression enriched for genes associated with proliferation, resembling clusters 0 and 1 from HT-29 (Supplementary Fig. S8C right). Because our data indicate

that β-catenin and MAPK signaling outputs modulate sensitivity to LB-100 (Fig. 1D; Supplementary Fig. S2), we also computed the activity of these pathways at the single-cell level in parental and combination-resistant cells (see Methods). No clear difference in the MAPK pathway activity scores was observed between parental and resistant HT-29 cells (Supplementary Fig. S9A top left), whereas SW-480-R scored slightly higher than SW-480 parental cells (Supplementary Fig. S9B, top left). On the other hand, β-catenin pathway scores were lower in the resistant cells from both models (Supplementary Fig. S9A and S9B, top right). Furthermore, we can observe on the UMAPs that lower MYC target scores mostly correspond to combination-resistant cells (Supplementary Fig. S9A and S9B, bottom left), indicating a decreased MYC activity. Likewise, we found lower E2F target pathway activity scores on HT-29 and SW-480 cells that acquired resistance to LB-100 + adavosertib (Supplementary Fig. S9A and S9B, bottom right). This is noteworthy because elevated expression of E2F targets is frequent in tumors, and higher levels have been associated with poor prognosis in different cancers (43). Overall, the single-cell RNA-seq data support the notion that acquired resistance to the drug combination results in reduced mitogenic signaling and attenuation of the proliferative transcriptional program characteristic of cancer cells.

The above data showing downmodulation of oncogenic signaling, reduced aneuploidy, and transcriptional shifts associated with less proliferative phenotypes suggest an intriguing outcome for the acquired resistance to the combination of LB-100 and adavosertib: suppression of the malignant phenotype. Anchorage-independent proliferation is a common trait of transformed cells and can be used as a proxy for malignancy. Therefore, we asked how acquired resistance to this combination would impact anchorage-independent proliferation in these colorectal cancer models in the absence of the drugs. Parental SW-480 cells showed similar endpoint viability both in attached or anchorage-independent conditions. Strikingly, the anchorage-independent proliferation of SW-480-R cells was around 10-fold lower than measured for the parental cells. (Supplementary Fig. S10A, right). Similar results were observed in HT-29 cells. However, these cells showed a lower anchorage-independent proliferation, compressing the comparative difference between parental and resistant cells (Supplementary Fig. S10A, left). Finally, we directly addressed the notion of reduced tumorigenicity associated with the acquired resistance. We transplanted SW-480 parental (which showed better anchorage-independent growth) and SW-480-R cells into immunocompromised mice and monitored tumor growth. The results showed clear engraftment within the first 25 days and steady tumor growth in mice transplanted with SW-480 parental cells. Conversely, SW-480-R cells either failed to develop or developed small tumors over 50 days after transplantation (Fig. 7D). The mice were sacrificed at the ethical endpoint of 1,500 mm³. Kaplan–Meier survival curves show that none of the 10 tumors from mice injected with SW-480-R cells reached that endpoint during the 3 months of the experiment. In contrast, 7 out of 9 tumors from parental SW-480 cells reached the 1,500 mm³ endpoint during the experiment (Fig. 7E). Spider plots further illustrate the poor engraftment of the combination-resistant cells compared with the parentals, despite evident

heterogeneity on the growth kinetics of the individual tumors (Supplementary Fig. S10B).

Together, these data indicate that chronic exposure to the LB-100 and adavosertib combination may lead to acquired resistance that is fundamentally distinct from what is seen with drugs that inhibit oncogenic signaling: suppression of the malignant phenotype.

DISCUSSION

We explored here an unconventional rationale for cancer therapy based on further activation of oncogenic signaling rather than trying to inhibit it. This approach is inspired by mounting experimental data indicating that the homeostasis of cancer cells relies on optimal levels of oncogenic signaling, not necessarily the highest level (4–6, 9). To support the malignant state, stress response pathways act as buffers to the detrimental effects of oncogenic signaling (8, 9). In the present study, we used the PP2A inhibitor LB-100 to hyperactivate oncogenic signaling, leading to multiple stresses in colorectal cancer cells. Using both compound and genetic screens, we found that concomitant inhibition of the mitotic gatekeeper kinase WEE1 is lethal in multiple cancer models, and this combination restrained the growth of patient-derived tumors in mice.

That deliberate overactivation of oncogenic signaling is toxic to cancer cells is not without precedent. For instance, pharmacologic upregulation of β-catenin and c-MYC by GSK-3β inhibition triggered apoptosis in RAS-driven cancer cells and suppressed tumor growth (44). More recently, it has been shown that upregulation of the WNT/β-catenin pathway can also be toxic in the context of loss-of-function APC mutations (45). Likewise, we have shown previously that MAPK activation induced by FGF2 is also detrimental to KRAS-driven cancer cells and leads to replication stress in an oncogenic KRAS-dependent manner (46). MAPK pathway activity is suppressed by DUSP-mediated (dual-specificity phosphatases) dephosphorylation (47). Inhibition of DUSP1/6 induced toxic levels of MAPK activity and triggered cell death in a panel of *Egfr-* and *Kras*-driven lung adenocarcinoma cells (48). Along the same lines, PP2A phosphatases suppress different oncogenic pathways, and previous data show that inhibition of these phosphatases by LB-100 is toxic to multiple cancer models (14). Our data confirm the activation of oncogenic signaling and stress response pathways induced by LB-100. Notably, despite the multitude of cellular processes in which PP2A is implicated (11, 12), unbiased analyses of our CRISPR screens place WNT/β-catenin and MAPK signaling at the core of LB-100 toxicity. Because many of the "stress hallmarks" of cancer (8) were mobilized by LB-100 in colorectal cancer cells, the tailored stress-focused drug library was instrumental in identifying CHK1 and WEE1 as LB-100 synthetic lethality targets. We focused on WEE1 in follow-up experiments because of the superior clinical development of WEE1 inhibitors compared with those targeting CHK1 (24).

We observed synergy between LB-100 and the WEE1 inhibitor adavosertib across different colon cancer, pancreatic cancer, and cholangiocarcinoma cell models. This suggests there is not a strong context dependency for this drug combination,

facilitating future clinical development. Synergy *in vitro* does not necessarily translate into synergy *in vivo*. Yet, we found higher synergy scores when adavosertib is combined with LB-100 compared with combinations with doxorubicin or gemcitabine across the models tested. This is noteworthy because modest single-drug efficacy has hindered the clinical development of adavosertib and other WEE1 inhibitors so far. Combinations with chemotherapy tend to increase efficacy but also toxicity (49). In preclinical models, LB-100 improved the efficacy of chemotherapy drugs without compounding the toxicity (14). This may point toward a better toxicity profile for the LB-100 + adavosertib combination in patients.

The mitotic defects observed are in agreement with previous studies using WEE1 inhibitor combinations. For instance, Aarts and colleagues showed that adavosertib forces S-phase cells into premature mitoses if DNA replication is stalled by gemcitabine (32). PARP (50) or ATR (51) inhibitors also result in replication stress and lead to similar aberrant mitoses in combination with WEE1 inhibition. Mechanistically, these studies have in common the induction of replication stress, priming cancer cells for defective mitoses. In our models, LB-100 also induced replication stress, and the combination with adavosertib led to premature mitoses. Downregulation of DNA-repair signaling has been proposed to underlie the replication stress induced by LB-100 (52). Furthermore, PP2A regulates various mitotic proteins, and LB-100 has been shown to induce mitotic catastrophe by deregulating the activity of these proteins (53). However, the upregulation of oncogenic signaling per se is sufficient to trigger both replication stress (54) and a myriad of mitotic defects (55, 56). This notion aligns with our data showing that WNT/β-catenin and MAPK signaling modulate LB-100 toxicity. Identifying the precise mechanistic contribution of each of these effects of LB-100 to the synergy with adavosertib requires further research. Nonetheless, our data show complementary effects of LB-100 and adavosertib on replication stress and mitosis, explaining the efficacy of the combination, and supporting further clinical investigation.

That the LB-100 and adavosertib combination showed synergy and no clear context dependency in the cancer models tested is promising, but it also raises questions about efficacy versus toxicity *in vivo*. Both drugs have been tested in animal models and clinical trials (14, 28) but not in this combination. In our study, we found consistent tumor suppression for the combination in clinically relevant colorectal cancer and CCA patient-derived tumors, despite different genetic backgrounds, previous treatments, and tissue of origin. Moreover, the fact that the three orthotopic colorectal cancer PDXs showed histopathologic regression with a reduced proportion of cancer cells in the tumor when treated with the combination is encouraging. The combination was tolerated in immunodeficient mice; however, tolerability in mice does not always translate to humans, and the safety of this combination must be carefully addressed in the clinic.

A potential concern of the approach proposed here is that activation of oncogenic signaling might cause normal or precancerous cells to proliferate in patients. However, normal cells have effective feedback mechanisms to limit oncogenic activity and uncontrolled proliferation. Higher levels of oncogenic signaling and less effective feedback to control that

signaling are hallmarks of cancer (1). Consistent with that notion, activation of the WNT/β-catenin pathway by Lithium Chloride (LiCl) suppressed the outgrowth of premalignant adenomas driven by APC loss in transgenic mouse models (57). More importantly, epidemiologic analyses revealed that long-term treatment of bipolar disorder patients with LiCl resulted in reduced risk of cancer (58). This scenario suggests that therapeutic hyperactivation of oncogenic signaling would not have tumor-inducing effects on normal or even precancerous cells. The favorable toxicity profile for LB-100 (16) in a phase I clinical trial and our current *in vivo* data also point toward a potential therapeutic window to exploit this concept clinically. Nonetheless, additional long-term *in vivo* experiments and the use of genetically engineered animal models can be instrumental to further derisk this approach.

Arguably the most appealing aspect of the therapeutic approach described here is that the stress cancer cells need to evade to become resistant is the hyperactivated oncogenic signaling itself. As such, the therapy could select for secondary events that reduce oncogenic signaling and attenuate the malignant phenotype. Indeed, we found downmodulation of oncogenic signaling and reduced proliferation in colorectal cancer models after acquiring resistance to the combination. Surprising also was the reduced aneuploidy, a common trait of malignant cells, observed in these combination-resistant cells compared with their parental counterparts. Analyzing the transcriptional "identity" of individual cells after acquired resistance revealed an overall trend toward less malignant phenotypes, despite evident heterogeneity. It is reasonable to assume that these different adaptations identified here (reduced aneuploidy, reduced WNT/β-catenin, MYC, and E2F signaling) cooperate to reduce the tumorigenicity of these resistant cells that we observed *in vivo*. How prevalent this tumor-suppressive acquired resistance will be across different cancer models and drugs activating oncogenic signaling remains to be investigated. Our data are consistent with a model in which further reinforcement of the very oncogenic signaling that underlies the oncogenic phenotype may force the cancer cells to give up signals that fuel oncogenic proliferation to escape the therapy.

METHODS

Cell Lines and Culture

The human cell lines SW-480, HT-29, DLD1, HCT116, LoVo, RKO, AspC-1, MIA-PaCa-2, PANC-1, YAPC, EGI-1, BJ, and SSP-25 were obtained from ATCC. DiFi cell lines were a gift from Alberto Bardelli. HaCaT cells are part of the Bernards' Lab cell line collection. The rat neuroblastoma cells B104 parental, B104-NMYC-C6A, and B104-NMYC-C78 have been previously published (21) and are also part of the Bernards lab cell line collection. HuCC-T1 and RBE cell lines were provided by Erasmus University. All cell lines were cultured in RPMI medium (except EGI-1, BJ, and HaCaT, which were cultured in DMEM), supplemented with 10% FBS, 1% penicillin/streptomycin and cultured at 37°C in 5% CO_2. The cell lines were authenticated by short-tandem-repeat DNA profiling. *Mycoplasma* tests were performed every 2 to 3 months. HT-29– and SW-480–resistant cells (HT-29-R and SW-480-R) were established by culturing the parental cells in the presence of increasing concentrations of the combination of LB-100 and adavosertib, up to the maintenance concentrations of 6 µmol/L LB-100 and 600 of nmol/L adavosertib.

shRNA Constructs

The lentiviral PP2AR1A shRNA vectors were retrieved from the arrayed TRC human genome-wide shRNA collection.

#1TRCN0000231508 CCGGCTACGCTCTTCTGCATCAATGCTC
GAGCATTGATGCAGAAGAGCGTAGTTTTTG
#2TRCN0000231509 CCGGTTGCCAATGTCCGCTTCAATGCTC
GAGCATTGAAGCGGACATTGGCAATTTTTG

Dose-Response Assays

All drug-response assays were performed in triplicate, using black-walled 384-well plates (Greiner #781091). Cells were plated with a 20% density (approximately) and incubated overnight for attachment. Drugs were then added to the cells using the Tecan D300e digital dispenser. 10 µmol/L phenylarsine oxide was used as positive control (0% cell viability) and DMSO was used as negative control (100% cell viability). Three to 5 days later, resazurin (Sigma #R7017) was added to the plates. After 1 to 4 hours of incubation (depending on the cell line), fluorescence ($560_{Ex}/590_{Em}$) was recorded using the EnVision (PerkinElmer).

Compounds

LB-100 #206834 and adavosertib (MK-1775) #201912 were purchased from Medkoo Biosciences. GDC-0575 #HY-112167A, doxorubicin #HY-15142, and gemcitabine #HY-17026 were purchased from MedChemExpress.

IncuCyte-based Proliferation and Caspase-3/7 Activity Assays

All IncuCyte assays were performed at least in triplicate, using black-walled 96-well plates (Greiner #655090). Cells were plated at a low density and incubated until attachment. Plates were then placed in the IncuCyte ZOOM (Essen Bioscience), which imaged the cells every 4 hours. Approximately 12 to 16 hours after plating, drugs were added to the cells using the Tecan D300e digital dispenser, as indicated. Phase-contrast images were collected and analyzed to detect cell proliferation based on confluence. When indicated, IncuCyte Caspase-3/7 green apoptosis assay reagent (Essen Bioscience #4440) was also added to the culture medium. Here, green fluorescent images were also collected and analyzed (by dividing the detected green fluorescence confluence by the phase-contrast confluence) to detect caspase-3/7 activity as a proxy for apoptosis.

Crystal Violet Long-term Viability Assays

Cells were plated at a low density in 12-well plates and incubated overnight for attachment. Drugs were then added to the cells using the Tecan D300e digital dispenser, as indicated. The culture media/drugs were refreshed every 2 to 3 days. When control wells were confluent, cells were fixed and stained for 20 to 30 minutes using a 1% formaldehyde (Millipore #104002)/1% methanol (Honeywell #32213)/0.05% crystal violet (Sigma #HT90132) solution in phosphate-buffered saline (PBS). Plates were then washed in water and left to dry before scanning.

Attached vs. Anchorage-Independent Proliferation Assays

For HT-29, an equal number of cells were plated in parallel on regular 12-well plates (TPP #92006) for attached proliferation; and on cell-repellent 12-well plates (Costar #3471) for anchorage-independent proliferation. The same procedure was used for SW-480 cells but using 96 wells (Greiner #655180) for attached and 96 wells (Greiner #655970) for anchorage-independent proliferation. After 5 to 6 days, the same initial numbers of cells were seeded in previously empty wells to provide the respective T0 readings. CellTiter-Glo 3D (Promega #G9682) was then used according to the manufacturer's protocol to estimate the relative endpoint cell proliferation in both growth conditions. Results are expressed in fold change over T0.

Synergy Matrices

All synergy matrices were performed in triplicate, using black-walled 384-well plates (Greiner #781091). Cells were plated at 10% to 20% density and incubated overnight for attachment. Drugs were then added to the cells using the Tecan D300e digital dispenser. 10 μmol/L phenylarsine oxide was used as positive control (0% cell viability) and DMSO was used as negative control (100% cell viability). 5 days later, resazurin (Sigma #R7017) was added to the plates. After 1 to 4 hours of incubation (depending on the cell line), fluorescence ($560_{Ex}/590_{Em}$) was recorded using the EnVision (PerkinElmer). The readings were then normalized using the positive and negative controls to express the relative viabilities. The normalized values for each concentration of single drugs or drug combinations were uploaded on https://synergyfinder.orgto calculate the respective synergy scores (ZIP).

Western Blots

After the indicated culture period and drug treatment, cells were washed with cold PBS, then lysed with RIPA buffer (25 mmol/L Tris-HCl, pH 7.6, 150 mmol/L NaCl, 1% NP-40, 1% sodium deoxycholate, 0.1% SDS) containing Complete Protease Inhibitor cocktail (Roche) and phosphatase inhibitor cocktails II and III (Sigma). Samples were then centrifuged for 15 minutes at 15,000 × *g* at 4°C and supernatant was collected. Protein concentration of the samples was normalized after performing a bicinchoninic acid (BCA) assay (Pierce BCA, Thermo Scientific), according to the manufacturer's instructions. Protein samples (denatured with DTT followed by 5 minutes of heating at 95°C) were then loaded in a 4% to 12% polyacrylamide gel. Gels were run (SDS-PAGE) for approximately 40 minutes at 180 volts. Proteins were transferred from the gel to a nitrocellulose membrane at 350 mA for 90 to 120 minutes. After the transfer, membranes were incubated in blocking solution (1% BSA/1% nonfat dry milk in TBS with 0.1% Tween-20 (TBS-T). Subsequently, membranes were probed with the primary antibodies in 5% bovine serum albumin (BSA) overnight at 4°C. Membranes were then washed 3 times for 10 minutes with TBS-T, followed by 1-hour incubation at room temperature with the secondary antibody (HRP conjugated) in a blocking solution. Membranes were again washed 3 times for 5 minutes in TBS-T. Finally, a chemiluminescence substrate (ECL, Bio-Rad) was added to the membranes and the signal was imaged using the ChemiDoc-Touch (Bio-Rad).

The following antibodies were purchased from Cell Signaling Technology: GAPDH #5174, Phospho-p44/42 MAPK (Erk1/2; Thr202/Tyr204) #4377, p44/42 MAPK (Erk1/2) #4695, Phospho-c-Jun (Ser73) #3270, c-Jun #2315, Phospho-4E-BP1 (Thr37/46) #2855, 4E-BP1 #9644, Active β-Catenin (non-phospho; Ser33/37/Thr41) #8814, β-Catenin #9562, Axin2 #2151, Phospho-Histone H2A.X (Ser139) #2577, Histone-H2A.X #7631, Histone H3 #4499, Phospho-Chk1 (Ser345) #2348, Chk1 #2360, IRE1α (14C10) #3294, HIF1α #3716, PARP #9542, and c-Myc #5605. The antibodies α-Tubulin #T9026 and Vinculin #V9131 were purchased from Sigma-Aldrich. Phospho-IRE1 alpha (Ser724) #PA1-16927 and PPP2R1A (703567) were purchased from Thermo Fisher. BCL9 L #ab113110 was purchased from Abcam. Phospho-Histone H3 (Ser10) #06-570 was purchased from MERCK (Upstate).

Stress-Focused Drug Screens

To compose the stress-focused drug library, we considered the following stresses often associated with malignant phenotypes: DNA damage stress, oxidative stress, mitotic stress, proteotoxic stress, metabolic stress, and senescence/apoptosis evasion (8). Each compound was selected based on published data showing either induction of the respective stress or inhibition of the cellular responses to it. The range of doses was tailored according to published data about the compound when available. On day 0, HT-29 or SW-480 cells were plated in black-walled 384-well plates (Greiner #781091) at 10% to 20% confluence. On the next day, the plates were divided into control and LB-100-treated arms. LB-100 (2.5 μmol/L) was added to the LB-100–treated arms and then each compound was added to both arms in 15 different doses without replicates using the MICROLAB STAR liquid handling workstation (Hamilton). In each plate, phenylarsine oxide (10 μmol/L) was used as positive control (0% cell viability) and DMSO was used as negative control (100% cell viability). After 3 days, resazurin (Sigma #R7017) was added to the plates. After 1 to 2 hours of incubation, fluorescence ($560_{Ex}/590_{Em}$) was recorded using the EnVision (PerkinElmer). The readings of each plate were then normalized using the positive and negative controls already taking into account any effect of LB-100 alone. The normalized values of each drug/dose were used to build drug–response curves in the absence or presence of LB-100. The AUC difference for each compound in the presence of LB-100 (2.5 μmol/L) relative to untreated controls is shown.

RNA-seq and Gene Set Enrichment Analysis

After plating and attachment overnight, HT-29 and SW-480 cells were treated with LB-100 (2.5 μmol/L) for the indicated time points. For harvesting, the cells were scraped into 15 mL tubes, washed once with cold PBS, and homogenized in RLT buffer (Qiagen #79216). Total RNA was isolated using the RNeasy Mini Kit (74106, Qiagen) including an on-column DNase digestion (79254, Qiagen), according to the manufacturer's instructions. Quality and quantity of the total RNA were assessed on the 2100 Bioanalyzer instrument following the manufacturer's instructions "Agilent RNA 6000 Nano" (G2938-90034, Agilent Technologies). Total RNA samples were subjected to TruSeq stranded mRNA library preparation, according to the manufacturer's instructions (Document #1000000040498 v00, Illumina). The stranded mRNA libraries were analyzed on a 2100 Bioanalyzer instrument following the manufacturer's protocol "Agilent DNA 7500 kit" (G2938-90024, Agilent Technologies), diluted to 10 nmol/L and pooled equimolar into multiplex sequencing pools for paired-end sequencing on the NovaSeq 6000 Illumina sequencing instrument. Paired-end sequencing was performed using 54 cycles for Read 1, 19 cycles for Read i7, 10 cycles for Read i5, and 54 cycles for Read 2, using the NovaSeq6000 SP Reagent Kit v1.5 (100 cycles; 20028401, Illumina). For the analysis, the RNA-seq count data were normalized using a relative total size factor. The data set was then filtered for protein-coding genes. Log$_2$ fold change and mean values were calculated for each time point of treatment compared with untreated. Before running a specific GSEA, the data were filtered for low counts using a filter of mean greater or equal to 10 in order to obtain robust scores. A GSEA for the Hallmarks gene set and KEGG gene set of the molecular signature database (59) was performed using the R-package fGSEA (BioRxiv, 2021.10.1101/060012), which calculates a NES score and a *P* value (59).

Single-cell RNA-seq

The single-cell RNA-seq data were generated in four runs: HT-29 treatment parental (S1), HT-29 combination-resistant (S2), SW-480 parental (S3), and SW-480 combination-resistant (S4). Parental cells were harvested untreated and resistant cells were harvested 24 hours after the washout of the drugs. For the single-cell 5′ sequencing library preparation, the Chromium Controller platform of 10X Genomics was used for single-cell partitioning and barcoding. Each cell's transcriptome was barcoded during reverse transcription, pooled cDNA was amplified, and Single-Cell 5′ Gene-Expression libraries were prepared according to the manufacturer's protocol (CG000331 Rev C, 10X Genomics). All libraries were quantified and normalized based on library QC data generated on the Bioanalyzer system according to the manufacturer's protocols (G2938-90321 and G2938-90024, Agilent Technologies). Based on the expected target cell counts, a balanced library pool of all samples was composed. The Single-Cell 5′ Gene-Expression library pool was quantified by qPCR, according to the KAPA Library Quantification Kit Illumina Platforms protocol (KR0405,

KAPA Biosystems). Paired-end sequencing was performed on a No-vaSeq 6000 Instrument (Illumina) using a NovaSeq 6000 S1 Reagent Kit v1.5 100 cycles (cat. no. 20028319, Illumina), using 26 cycles for Read 1, 10 cycles for Read i7, 10 cycles for Read i5, and 92 cycles for Read 2. This resulted in an average sequencing depth of 65.000 median reads per cell.

The resulting data were then transformed to FASTQ format and aligned to the reference genome (*Homo sapiens* hg38) using the commercial CellRanger 7.0.1 pipeline. For the downstream bioinformatic analyses, we used the following pipeline per cell line: According to standard QC metrics (RNA content, mitochondrial percentage), cells with low quality were first filtered out, and potential doublets were removed using scDblFinder (v1.10.0) (60). Data set were then integrated using the Seurat CCA alignment strategy (v4.2.0; ref. 61), which yielded both UMAP projections (62) and Leiden clusters (63). Cluster-specific markers were derived using DESeq2 (v1.36.0; ref. 64) and cluster-specific enrichment was assessed using the GSEApy (v1.0.1) EnrichR pipeline (65, 66). Finally, we estimated pathway activity scores using UCell (v2.0.1; ref. 67).

CRISPR Screens

CRISPR Knockout Screens. The appropriate number of cells to achieve a 250-fold representation of the Brunello library for all the screen arms and replicates were transduced at approximately 50% confluence in the presence of polybrene (8 μg/mL) with the appropriate volume of the lentiviral-packaged sgRNA library. Cells were incubated overnight, followed by the replacement of the lentivirus-containing medium with fresh medium containing puromycin (2 μg/mL). The lentivirus volume to achieve a multiplicity of infection (MOI) of 0.3, as well as the puromycin concentration to achieve a complete selection in 3 days, was previously determined. After puromycin selection, cells were split into the indicated arms/replicates (for each arm, the appropriate number of cells to keep a 250-fold representation of the library was plated at approximately 10%–20% confluence) and a T0 (reference) time point was harvested. Cells were maintained as indicated and, in case a passage was required, cells were reseeded at the appropriate number to keep at least a 500-fold representation of the library. Cells were harvested after about 8 population doublings, washed with PBS, pelleted, and stored at −80°C until DNA extraction.

Genomic DNA was extracted (Zymo Research, D3024) from cell pellets according to the manufacturer's instructions. For every sample, DNA was quantified and the necessary DNA to maintain a 250-fold representation of the library was used for subsequent procedures (for this, we assumed that each cell contains 6.6 pg genomic DNA). Each sample was divided over 50 μL PCR reactions (using a maximum of 1 μg genomic DNA per reaction) using barcoded forward primers to be able to deconvolute multiplexed samples after next-generation sequencing. PCR mixture per reaction: 10 μL 5× HF Buffer, 1 μL 10 μmol/L forward primer, 1 μL 10 μmol/L reverse primer, 0.5 μL Phusion polymerase (Thermo Fisher, F-530XL), 1 μL 10 mmol/L dNTPs, adding H2O and template to 50 μL. Cycling conditions: 30 seconds at 98°C, 20× (30 seconds at 98°C, 30 seconds at 60°C, 1 minutes at 72°C), 5 minutes at 72°C. The products of all reactions from the same sample were pooled, and 2 μL of this pool was used in a subsequent PCR reaction using primers containing adapters for next-generation sequencing. The same cycling protocol was used, however this time for 15 cycles. Next, PCR products were purified using the Bioline ISOLATE II PCR and Gel Kit (GC Biotech, BIO-52060) according to the manufacturer's instructions. DNA concentrations were measured and, based on this, samples were pooled equimolarly.

The pool of amplified sgRNA sequences was sequenced on an Illumina HiSeq 2500 with a high-output kit (Single-Read, 65 bp). The reads were mapped to the unique barcodes used for each sample and sgRNA sequences of the Brunello library. Mapped read counts were subsequently used as input for further analyses.

CRISPRa Screen. HT29 dCas9-VP64 cells were generated by lentiviral transduction of HT29 cells with Lenti-dCas9-VP64-Blast (Addgene, 61425) in the presence of 8 μg/mL polybrene (Santa Cruz, sc-134220A) and subsequent selection with 10 μg/mL blasticidin (In-vivoGen, ant-bl). Clonal derivatives of the HT-29 dCas9-VP64 cell line were established by limited dilution.

HT29 dCas9-VP64 clone E cells were transduced with lentivirus of Calabrese pooled human CRISPRa library sets A and B (Addgene, 92379 and 92380) separately, in the presence of 8 μg/mL polybrene (Santa Cruz, sc-134220A), and at an MOI of approximately 0.3. Following 3 days of selection with 2 μg/mL puromycin (Gibco, A11138-03), reference samples were collected (*t* = 0), and cells were separated into different treatment arms. Cells were subsequently cultured in the presence of 5 μmol/L LB-100 (2 and 3 replicates for sets A and B, respectively) or DMSO (vehicle control; 3 replicates for each set) while maintaining at least 16 million cells per replicate at all times, ensuring a 250-fold representation of each library set. After both arms reached at least 12 population doublings, cells were collected and stored as pellet at −80°C.

Genomic DNA was isolated using the Gentra Puregene kit (Qiagen, 158767) following the manufacturer's protocol specified for cultured cells, and dissolved in the hydration solution overnight while shaking at room temperature. DNA yield ranged from 216 to 486 μg per sample. The genomic DNA was divided into multiple reactions per sample (50 μg each, using all material) and fragmented at 37°C overnight, using 100 U Ndel enzyme (R0111L) and 50 μL 10X cutSmart buffer (B7204S) from New England Biolabs, supplemented to 500 μL with nuclease-free water (Thermo Fisher, AM9932). The reactions were heated to 100°C for 10 minutes, and following the addition of 500 μL 2 mol/L NaCl, reheated to 100°C for 5 minutes and then immediately snap-frozen in liquid nitrogen. Per tube and prior to thawing, 1 μL of each 10 μmol/L 5′ biotinylated capture oligo (TGCTTACC GTAACTTGAAAGTATTTCGATTTCTTGGCTTTATATATCTTG and TGCTCTCGTGGAGAGGAGCGACGCCATATCGTCTGCTCC CTCGTATTCGC) was added on top of the frozen solution, which was then immediately transferred to a thermoshaker for overnight hybridization at 60°C. To capture hybridized DNA encoding sgRNA sequences, 20 μL Streptavidin T1 Dynabeads (Thermo Fisher, 65602) were washed three times with 500 μL wash buffer (1 M NaCl, 10 mmol/L Tris-HCl, pH 8), added to each tube, and incubated under rotation at room temperature for 2 hours. The beads were washed twice with wash buffer and twice with 10 mmol/L Tris-HCl (pH 8). Nonhybridized biotinylated oligonucleotides were digested in 50 μL reactions composed of 44 μL 10 mmol/L Tris-HCl (pH 8), 5 μL 10X Exonuclease buffer, and 1 μL Exonuclease I (New England Biolabs, M0293L), at 37°C for 1 hour. Beads were washed 3 times with 10 mmol/L Tris-HCl (pH 8) and resuspended in 20 μL 10 mmol/L Tris-HCl (pH 8).

Two rounds of PCR were performed to amplify the sgRNA sequences. In the first PCR, distinct forward primers that each encodes a unique barcode sequence and facilitates deconvolution of sequence reads of pooled samples (ACACTCTTTCCCTACACGACGCTCTTC CGATCTNNNNNNGGCTTTATATATCTTGTGGAAAGGACG with NNNNNN representing barcode sequences CGTGAT, ACATCG, GC CTAA, TGGTCA, AAGCTA, GTAGCC, and TACAAG) were used in combination with a common reverse primer (GTGACTGGAGTTCAGAC GTGTGCTCTTCCGATCTCGACGCCATATCGTCTGCT). PCR mixture: 1 μL 10 μmol/L forward primer, 1 μL 10 μmol/L reverse primer, 1 μL 10 mmol/L dNTPs (Thermo Fisher, R0193), 0.5 μL Phusion polymerase and 10 μL 5× HF buffer (New England Biolabs, M0530L), supplemented with nuclease-free water to a total volume of 50 μL. PCR cycling conditions: 3 minutes at 98°C, 20 times (30 seconds at 98°C, 30 seconds at 60°C, 30 seconds at 72°C), and 5 minutes at 72°C. Per sample, products of individual reactions were pooled, and 2 μL of each pool was used as a template in the second PCR with conditions similar to the first, but having 15 instead of 20 cycles, to add the p5 and p7 adapter

sequences as well as unique indices to discriminate samples of the Calabrese library set A and B (primers: AATGATACGGCGACCAC CGAGATCTACACTCTTTCCCTACACGACGCTCTTCCGATCT and CAAGCAGAAGACGGCATACGAGATNNNNNNGTGACTGGA GTTCAGACGTGTGCTCTTCCGATCT with NNNNNN representing index sequence ACATCG and GCCTAA). The PCR products were purified using the Bioline ISOLATE II PCR and Gel kit (GC Biotech, BIO-52060) following the manufacturer's protocol and pooled by combining 150 ng of each sample.

The pool of amplified sgRNA sequences was sequenced on an Illumina NextSeq with a high-output kit (Single-Read, 75 bp). The reads were mapped to the unique barcode and index combination used for each sample and sgRNA sequences of both Calabrese library sets. Mapped read counts were subsequently used as input for further analyses.

Bioinformatics Analysis For both types of CRISPR screens, the sequence count data were normalized using a relative total size factor. Statistical comparisons of the conditions treated versus untreated were performed using drugZ (68). Log$_2$ fold changes were calculated based on the median of each of the two conditions. The first criterion for hit selection was a drugZ FDR smaller than or equal to 0.25 in treated/untreated comparison. In addition, for negative selection, log$_2$ fold change of treated/untreated should be smaller than or equal to -1. For positive selection, those should be greater than or equal to 1.

String Network Analysis

The full list of hits from both CRISPR screens shown in Supplementary Fig. S2 was inputted on the STRING web tool (https://string-db.org) and analyzed using the default settings. The top 5 GO Biological Processes and Molecular Functions with their respective FDRs are shown.

Time-Lapse Microscopy

Cells were plated on 8-well glass-bottom dishes (LabTek) and incubated overnight for attachment. Drugs were then added as described and the cells were imaged using a Deltavision deconvolution microscope equipped with a heat chamber. For DNA visualization, cells stably expressed H2B-GFP (obtained by retroviral infection). Images were acquired every 5 minutes using a 203 (0.25 NA) objective. Z-stacks were acquired with 2-mm intervals. Images were analyzed and processed using Softworx and ImageJ.

Immunofluorescence Staining

Cells were plated on 12-mm glass coverslips and incubated overnight for attachment. After the indicated treatments, the cells were fixed for 15 minutes at room temperature in 4% formaldehyde with 0.5% Triton X-100. The mouse anti-alpha-tubulin (Sigma, #t5168) was incubated overnight at 4°C. Secondary antibodies (Molecular probes, Invitrogen) and DAPI (1 µg/mL) were incubated for 2 hours at room temperature. Coverslips were mounted using ProLong Gold (Invitrogen). Images were taken on a THUNDER Imager 3D Cell Culture van Leica 63× oil lens: obj. HC PL APO 63×/1.40–0.60 OIL 11506349.

Chromosome Spreads

Chromosome spreads were prepared from HT-29 cells treated with inhibitors for 16 hours. After that, cells were treated with Nocodazole for 3 hours and harvested by mitotic shake-off. Cells were then incubated with 0.075 M of KCl at 37°C for 10 minutes and a drop of fixative (methanol:acetic acid, in a 3:1 ratio made fresh) was added followed by centrifugation at 1,500 rpm for 5 minutes. The supernatants were discarded and the cells were fixed with 1 mL of fixative

for 30 minutes, followed by fixative + DAPI (1 µg/mL). The cell suspensions were then dropped from a 5 cm distance onto an ethanol cleaned coverslips, dried at room temperature and the chromosome spreads were mounted with ProLong Gold (Invitrogen). Images were acquired using a Thunder deconvolution microscope (Applied Precision) with a 60 × 1.40 NA oil objective. Softworx (Applied Precision), ImageJ, Adobe Photoshop, and Illustrator CS6 were used to process acquired images.

Detection of BrdUrd Foci under Native DNA Conditions

For the detection of long fragments of single-stranded DNA (ssDNA), typical of replication stress, BrdUrd (50 mmol/L) was incorporated into the DNA of exponentially growing cells (HT-29 and SW-480) for 48 hours. After that, we washed the coverslips and added fresh media adding the drugs as indicated for 8 hours. Next, cells were fixed using 4% of paraformaldehyde in PBS and permeabilized with 0.2% Triton X-100. BrdUrd was detected (when accessible) using a purified mouse Anti-BrdUrd (BD Biosciences) followed by a secondary antibody goat anti-mouse conjugated to Alexa Fluor 488 (Thermo Scientific). To ensure that all cells incorporated BrdUrd, one additional coverslip for each condition analyzed was prepared to be subjected to DNA denaturation using 2 mol/L HCl (for 15 minutes), followed by a neutralization step with 0.1 mol/L Borate buffer (100 mmol/L H$_3$BO$_3$, 75 mmol/L NaCl, 25 mmol/L Na$_2$B$_4$O$_7$·10H$_2$O, pH = 7.4) for 10 minutes. Stained coverslips were mounted with Vectashield Mounting Medium with DAPI (Vector Labs). Images were captured using an Olympus BX51 fluorescence microscope coupled with a digital camera (XM10; Olympus) and analyzed using OLYMPUS CELL F software (version 5.1.2640). At least 100 cells were analyzed per coverslip.

DNA Fiber Assays

For the DNA fiber assays, after the indicated treatments, cells were labeled with CldU (25 µmol/L, 20 minutes) and IdU (250 µmol/L, 20 minutes). Labeled cells were lysed (200 mmol/L Tris-HCl pH 7.4, 50 mmol/L EDTA, 0.5% SDS), spread onto IHC Microscopy slides (Dako) and fixed for 10 minutes in methanol:acetic acid (3:1). Next, slides were incubated in HCl (2.5 M) for 1 hour and 15 minutes, washed with PBS and incubated in blocking solution (PBS + 1% BSA and 0.1% Tween 20) for 1 hour. Primary rat-anti-BrdUrd BU1/75 (1:500, Abcam) and mouse-anti-BrdUrd antibody Clone B44 (1:750, BD Biosciences) were incubated for 1 hour in blocking solution. After washing with PBS, primary antibodies were fixed for 10 minutes using 4% paraformaldehyde. Secondary antibodies (goat-anti-mouse Alexa Fluor 488 and goat-anti-rat Alexa Fluor 555 (both 1:500, Invitrogen) were incubated for 1.5 hours in a blocking solution. Finally, Menzel-Gläser coverslips were mounted onto the slides using Vectashield and imaged using a Zeiss AxioObserver Z1 inverted microscope using a Hamamatsu ORCA AG Black and White CCD camera.

Cell Cycle and p-H3 Flow Cytometry

For bromodeoxyuridine (BrdUrd)/propidium iodide cell-cycle analyses, after the indicated treatments, cells were harvested by trypsinization, washed with cold PBS, and then fixed in ice-cold 75% ethanol in PBS overnight at 4°C. BrdUrd (10 µmol/L) was added 1 hour before harvesting. Fixed cells were washed with PBS and treated with 5 mol/L HCl and 0.5% Triton-X100 for 20 minutes and then washed with 10 mL Tris-HCl (pH 7.5). Next, cells were incubated with mouse anti-BrdUrd (DAKO clone BU20A 1:40) for 1 hour. After washing with PBS, cells were incubated with polyclonal goat anti-mouse FITC (DAKO F0479 1:20). Finally, cells were washed and resuspended in PBS with propidium iodide (PI; 20 µg/mL) and RNase A (200 µg/mL), incubated at 37°C for 30 minutes and finally measured on the flow cytometer.

For phospho-histone H3 (S10) staining, cells were fixed as described above, washed in PBS, and incubated for 1 hour with the conjugated histone antibody (histone H3 S10 Millipore 06-570-AF488). Cells were then resuspended in a PI (50 µg/mL) + RNase A (10 µg/mL) solution in PBS for at least 20 minutes before analysis in the flow cytometer. For all flow cytometer experiments, data were acquired with Attune NxT flow cytometer (Life Technologies) and analyzed with FlowJo V.10 software (Treestar, Inc.). At least 20,000 cells per sample were analyzed.

Animal Models

Generation of Patient-Derived Orthotopic Xenografts from Colorectal Tumors and Drug Treatments. Primary tumors were obtained from Bellvitge Hospital (HUB) and the Catalan Institute of Oncology (ICO) with approval from the Ethical Committee (CEIC Bellvitge Hospital), ethical and legal protection guidelines for human subjects, including written informed consent, in accordance with the Declaration of Helsinki. The experimental design was approved by the IDI-BELL animal facility committee (AAALAC Unit1155) under approved procedure 9111. All animal experiments were performed following the guidelines for Ethical Conduct in the Care and Use of Animals as stated in the International Guiding Principles for Bio-medical Research Involving Animals, developed by the Council for International Organizations of Medical Sciences.

To establish the orthotopic colorectal cancer models from patients with refractory metastatic colorectal cancer, a small fragment of lung metastases [patient-derived orthotopic xenografts 1 and 2 (PDOX1 and PDOX2)] or a peritoneal implant [patient-derived orthotopic xenograft 3 (PDOX3)] from three different patients with colorectal cancer previously treated with fluoropyrimidines-based chemotherapy (see below) were obtained. Briefly, a small tumor piece of 2 to 4 mm³ maintaining tridimensional structure was anchored with Prolene 7.0 to the serosa of the caecum of two 5- to 6-week-old male athymic nude mice (strain Hsd:Athymic Nude-Foxn1nu) purchased from Envigo. After implantation, mice were inspected twice a week. At euthanasia, the tumors were harvested, cut into small fragments, and serially transplanted into new animals for tumor perpetuation or experimental treatment procedures.

PDOX 1 was generated from a lung metastasis of a male patient initially diagnosed with stage III colon adenocarcinoma (MSS, RAS, and BRAF WT). This patient received adjuvant Folfox (first line) and Folfiri + cetuximab (second line) upon liver relapse. A subsequent relapse in the liver was surgically removed. After subsequent liver and lung (from which the PDOX was generated) progression, Folfox + cetuximab (third line) were given, obtaining a partial response. PDOX 2 was generated from a lung metastasis of a male patient initially diagnosed with stage III left colon adenocarcinoma (MSS, RAS, and BRAF WT). This patient received adjuvant capecitabine (first line) and Folfox + panitumumab (second line) upon liver relapse. A subsequent relapse in the lung (from which the PDOX was generated) and adrenal gland were surgically removed. After a liver relapse, Folfiri + aflibercept (third line) was given as neoadjuvant therapy.

PDOX 3 was generated from a male patient initially diagnosed with stage IV colon adenocarcinoma (RAS WT, BRAF V600E mutant). This patient received Folfox as the first-line treatment (partial response) and cetuximab + encorafenib + binimetinib as the second-line (partial response). Upon relapse, a peritoneal implant sample was obtained to generate the PDX, and Folfiri + aflibercept was given as a third-line treatment (partial response).

For the treatment experiments, fragments of PDOX1 (*n* = 25 mice), PDOX2 (*n* = 17 mice), and PDOX3 (*n* = 25 mice) tumors were transplanted into the cecum of mice. When tumors reached a homogeneous palpable size (3–5 weeks), mice were randomly allocated into the treatment groups: vehicles; LB-100 (1.5 mg/kg); adavosertib (80 mg/kg); and LB-100 + adavosertib at the same doses. LB-100 was administered by intraperitoneal injection (i.p.) on days 1, 3, and 5, whereas adavosertib was administered by oral gavage (o.g.) on days 1 to 5 in 7-day cycles. For combined treatments, adavosertib was administered 2 to 3 hours after LB-100. Drugs were prepared fresh before each daily treatment. Adavosertib was formulated in 2% DMSO + 30% PEG 300 + 5% Tween 80 + ddH$_2$O, and LB-100 was dissolved in water. Four hours after the last treatment, mice were sacrificed, and tumors were collected, measured, and imaged. Tumor volumes based on caliper measurements were calculated using the modified ellipsoidal formula: tumor volume = ½ length × width². Representative tumor fragments were either frozen in nitrogen or fixed and then processed for paraffin embedding.

Toxicity Study. The heart, liver, lung, and spleen of mice implanted with PDOX1 and PDOX2 tumors treated with the different schemes have been studied histologically. A total of 5 animals treated with vehicle (3 PDOX1 and 2 PDOX2), 6 animals treated with adavosertib, 6 animals treated with LB-100, and 6 animals treated with the combination (3 PDOX1 and 3 PDOX2 in each treatment group) were studied. No histologic alterations were observed in these tissues in any mouse.

Cholangiocarcinoma PDXs. In compliance with the protocol approved by the Institutional Review Board of Naval Military Medical University Affiliated Eastern Hepatobiliary Hospital and with the written informed consent of the participant in accordance with the Declaration of Helsinki, fragments of surgically resected tumor tissues from a patient with ICC were used for xenotransplantation (PDX1 = CH-17-0005 FP6). In brief, patient samples were collected, trimmed, cut into 20 to 30-mm³ fragments and implanted subcutaneously in the fore flanks of anesthetized 6- to 8-week-old male BALB/c nude mice within 3 hours.

Tumor volumes based on caliper measurements were calculated using the modified ellipsoidal formula: tumor volume = ½ length × width². After the tumor volumes reached around 50 to 100 mm³, mice were randomized into the indicated treatment groups. LB-100 (intraperitoneal injection) was given on day 1, adavosertib (oral gavage) was given on days 1 to 3, in 4-day cycles. All procedures and protocols were approved by the Institutional Animal Care and Use Committee of Shanghai (IACUC NO. 2022-0025).

Engraftment of Parental versus Combination-Resistant Cells. The experiment was approved by the Animal Ethics Committee of the Netherlands Cancer Institute. SW-480 parental or SW-480 combination-resistant cells were resuspended in PBS and mixed 1:1 with matrigel (Corning 354230). Three million cells per mouse (*n* = 10 per group) were injected subcutaneously into the posterior right flanks of 7-week-old immunodeficient NMRI nude mice. Tumor size was measured 3 times a week by caliper and the volume was calculated by the modified ellipsoidal formula [tumor volume = ½(length × width²)]. Mice were sacrificed at the ethical endpoint of 1,500 mm³.

Statistics and Reproducibility

With the exceptions of CRISPR screens, drug screens, RNA-seq, and single-cell RNA-seq, each *in vitro* experiment has been independently reproduced with similar results. GraphPad Prism was used for the statistical analyses.

Data Availability

The CRISPR screen data generated are provided in Supplementary Tables S2, S3, and S7. The raw data can be provided upon request from the corresponding author. The bulk and single-cell RNA-seq data have been deposited in the Zenodo database (https://zenodo.org/records/10640576; https://zenodo.org/records/10623223). All

single-cell analysis codes have been deposited in the github repository (https://github.com/saroudant/paradoxical_activation_scrnaseq). All other data generated or analyzed during the study are available upon request from the corresponding author.

Authors' Disclosures

Authors' Contributions

M.H. Dias: Conceptualization, formal analysis, investigation, methodology, writing–original draft, writing–review and editing. **A. Friskes:** Investigation, methodology, writing–original draft, writing–review and editing. **S. Wang:** Data curation, formal analysis, investigation. **J.M. Fernandes Neto:** Data curation, formal analysis, investigation. **F. van Gemert:** Data curation, formal analysis, validation, investigation, methodology, writing–review and editing. **S. Mourragui:** Data curation, validation, investigation, methodology, writing–review and editing. **C. Papagianni:** Data curation, validation, investigation. **H.J. Kuiken:** Investigation, methodology. **S. Mainardi:** Data curation, formal analysis, validation. **D. Alvarez-Villanueva:** Data curation, Formal analysis, validation, investigation. **C. Lieftink:** Data curation, formal analysis, methodology, writing–review and editing. **B. Morris:** Data curation, validation. **A. Dekker:** Data curation, formal analysis, investigation. **E. van Dijk:** Data curation, investigation. **L.H. Wilms:** Investigation. **M.S. da Silva:** Data curation, supervision, validation. **R.A. Jansen:** Data curation, formal analysis, validation, investigation. **A. Mulero-Sanchez:** Data curation, formal analysis, investigation. **E. Malzer:** Data curation, formal analysis, validation, investigation. **A. Vidal:** Formal analysis, supervision, validation, investigation. **C. Santos:** Data curation, formal analysis, validation, investigation. **R. Salazar:** Data curation, formal analysis, validation, investigation. **R.A. Wailemann:** Data curation, validation, investigation. **T.E. Torres:** Data curation, formal analysis, supervision, validation, investigation. **G. De Conti:** Data curation, validation, investigation. **J.A. Raaijmakers:** Data curation, validation, investigation. **P. Snaebjornsson:** Data curation, formal analysis, methodology, writing–review and editing. **S. Yuan:** Data curation, supervision. **W. Qin:** Data curation, supervision. **J.S. Kovach:** Conceptualization, resources, supervision, validation, investigation. **H.A. Armelin:** Data curation, formal analysis, supervision, validation, investigation. **H. te Riele:** Data curation, formal analysis, supervision, validation, investigation, writing–review and editing. **A. van Oudernaarden:** Data curation, Supervision. **H. Jin:** Data curation, supervision, validation, investigation. **R.L. Beijersbergen:** Resources, data curation, formal analysis, supervision, validation, investigation, writing–review and editing. **A. Villanueva:** Resources, Data curation, formal analysis, supervision, validation. **R.H. Medema:** Resources, data curation, formal analysis, supervision, validation, writing–review and editing. **R. Bernards:** Conceptualization, supervision, funding acquisition, writing–original draft, writing–review and editing.

Acknowledgments

Note

REFERENCES

1. Hanahan D, Weinberg RA. The hallmarks of cancer. Cell 2000;100: 57–70.
2. Pagliarini R, Shao W, Sellers WR. Oncogene addiction: pathways of therapeutic response, resistance, and road maps toward a cure. EMBO Rep 2015;16:280–96.
3. Groenendijk FH, Bernards R. Drug resistance to targeted therapies: déjà vu all over again Mol Oncol 2014;8:1067–83.
4. Ito T, Young MJ, Li R, Jain S, Wernitznig A, Krill-Burger JM, et al. Paralog knockout profiling identifies DUSP4 and DUSP6 as a digenic dependence in MAPK pathway-driven cancers. Nat Genet 2021;53:1664–72.
5. Chan LN, Murakami MA, Robinson ME, Caeser R, Sadras T, Lee J, et al. Signalling input from divergent pathways subverts B cell transformation. Nature 2020;583:845–51.
6. Ecker V, Stumpf M, Brandmeier L, Neumayer T, Pfeuffer L, Engleitner T, et al. Targeted PI3K/AKT-hyperactivation induces cell death in chronic lymphocytic leukemia. Nat Commun 2021;12:3526.
7. Unni AM, Lockwood WW, Zejnullahu K, Lee-Lin SQ, Varmus H. Evidence that synthetic lethality underlies the mutual exclusivity of oncogenic KRAS and EGFR mutations in lung adenocarcinoma. eLife 2015;4:e06907.
8. Luo J, Solimini NL, Elledge SJ. Principles of cancer therapy: oncogene and non-oncogene addiction. Cell 2009;136:823–37.
9. Dias MH, Bernards R. Playing cancer at its own game: activating mitogenic signaling as a paradoxical intervention. Mol Oncol 2021;15: 1975–85.
10. Ciccone M, Calin GA, Perrotti D. From the biology of PP2A to the PADs for therapy of hematologic malignancies. Front Oncol 2015;5:21.
11. Thompson JJ, Williams CS. Protein phosphatase 2A in the regulation of Wnt signaling, stem cells, and cancer. Genes (Basel) 2018;9:121.
12. Reynhout S, Janssens V. Physiologic functions of PP2A: Lessons from genetically modified mice. Biochim Biophys Acta Mol Cell Res 2019; 1866:31–50.
13. Vainonen JP, Momeny M, Westermarck J. Druggable cancer phosphatases. Sci Transl Med 2021;13:eabe2967.
14. Hong CS, Ho W, Zhang C, Yang C, Elder JB, Zhuang Z. LB100, a small molecule inhibitor of PP2A with potent chemo-and radio-sensitizing potential. Cancer Biol Ther 2015;16:821–33.
15. Mazhar S, Taylor SE, Sangodkar J, Narla G. Targeting PP2A in cancer: combination therapies. Biochim Biophys Acta Mol Cell Res 2019; 1866:51–63.
16. Chung V, Mansfield AS, Braiteh F, Richards D, Durivage H, Ungerleider RS, et al. Safety, tolerability, and preliminary activity of LB-100, an inhibitor of protein phosphatase 2A, in patients with relapsed solid tumors: an open-label, dose escalation, first-in-human, phase I trial. Clin Cancer Res 2017;23:3277–84.
17. Muzny DM, Bainbridge MN, Chang K, Dinh HH, Drummond JA, Fowler G, et al. Comprehensive molecular characterization of human colon and rectal cancer. Nature 2012;487:330–7.

18. Szklarczyk D, Franceschini A, Wyder S, Forslund K, Heller D, Huerta-Cepas J, et al. STRING v10: protein–protein interaction networks, integrated over the tree of life. Nucleic Acids Res 2015;43:D447–52.

19. Lecarpentier Y, Schussler O, Hébert JL, Vallée A. Multiple targets of the canonical WNT/β-catenin signaling in cancers. Front Oncol 2019;9:1248.

20. Zhu J, Blenis J, Yuan J. Activation of PI3K/Akt and MAPK pathways regulates Myc-mediated transcription by phosphorylating and promoting the degradation of Mad1. Proc Natl Acad Sci U S A 2008;105:6584–9.

21. Bernards R, Dessain SK, Weinberg RA. N-myc amplification causes down-modulation MHC class I antigen expression in neuroblastoma. Cell 1986;47:667–74.

22. Wang L, Lankhorst L, Bernards R. Exploiting senescence for the treatment of cancer. Nat Rev Cancer 2022;22:340–55.

23. Bollen M, Peti W, Ragusa MJ, Beullens M. The extended PP1 toolkit: designed to create specificity. Trends Biochem Sci 2010;35:450–8.

24. Gorecki L, Andrs M, Korabecny J. Clinical candidates targeting the atr–chk1–wee1 axis in cancer. Cancers (Basel) 2021;13:795.

25. Yadav B, Wennerberg K, Aittokallio T, Tang J. Searching for drug synergy in complex dose-response landscapes using an interaction potency model. Comput Struct Biotechnol J 2015;13:504–13.

26. Bengtsson A, Andersson R, Ansari D. The actual 5-year survivors of pancreatic ductal adenocarcinoma based on real-world data. Sci Rep 2020;10:16425.

27. Yao D, Kunam VK, Li X. A review of the clinical diagnosis and therapy of cholangiocarcinoma. J Int Med Res 2014;42:3–16.

28. Ghelli Luserna Di Rorà A, Cerchione C, Martinelli G, Simonetti G. A WEE1 family business: regulation of mitosis, cancer progression, and therapeutic target. Hematol Oncol 2020;13:126.

29. De Witt Hamer PC, Mir SE, Noske D, Van Noorden CJF, Würdinger T. WEE1 kinase targeting combined with DNA-damaging cancer therapy catalyzes mitotic catastrophe. Clin Cancer Res 2011;17:4200–7.

30. Vitale I, Galluzzi L, Castedo M, Kroemer G. Mitotic catastrophe: a mechanism for avoiding genomic instability. Nat Rev Mol Cell Biol 2011;12:385–92.

31. Lindqvist A, Rodríguez-Bravo V, Medema RH. The decision to enter mitosis: feedback and redundancy in the mitotic entry network. J Cell Biol 2009;185:193–202.

32. Aarts M, Sharpe R, Garcia-Murillas I, Gevensleben H, Hurd MS, Shumway SD, et al. Forced mitotic entry of S-phase cells as a therapeutic strategy induced by inhibition of WEE1. Cancer Discov 2012;2:524–39.

33. Zeman MK, Cimprich KA. Causes and consequences of replication stress. Nat Cell Biol 2014;16:2–9.

34. Beck H, Nähse-Kumpf V, Larsen MSY, O'Hanlon KA, Patzke S, Holmberg C, et al. Cyclin-dependent kinase suppression by WEE1 kinase protects the genome through control of replication initiation and nucleotide consumption. Mol Cell Biol 2012;32:4226–36.

35. Elbæk CR, Petrosius V, Benada J, Erichsen L, Damgaard RB, Sørensen CS. WEE1 kinase protects the stability of stalled DNA replication forks by limiting CDK2 activity. Cell Rep 2022;38:110261.

36. Rodriguez-Acebes S, Mourón S, Méndez J. Uncoupling fork speed and origin activity to identify the primary cause of replicative stress phenotypes. J Biol Chem 2018;293:12855–61.

37. Ge XQ, Jackson DA, Blow JJ. Dormant origins licensed by excess Mcm2-7 are required for human cells to survive replicative stress. Genes Dev 2007;21:3331–41.

38. Ibarra A, Schwob E, Méndez J. Excess MCM proteins protect human cells from replicative stress by licensing backup origins of replication. Proc Natl Acad Sci U S A 2008;105:8956–61.

39. Duda H, Arter M, Gloggnitzer J, Teloni F, Wild P, Blanco MG, et al. A mechanism for controlled breakage of under-replicated chromosomes during mitosis. Dev Cell 2016;39:740–55.

40. Rubbia-Brandt L, Giostra E, Brezault C, Roth AD, Andres A, Audard V, et al. Importance of histological tumor response assessment in predicting the outcome in patients with colorectal liver metastases treated with neo-adjuvant chemotherapy followed by liver surgery. Ann Oncol 2007;18:299–304.

41. Kopetz S, Grothey A, Yaeger R, Van Cutsem E, Desai J, Yoshino T, et al. Encorafenib, binimetinib, and cetuximab in BRAF V600E–mutated colorectal cancer. N Engl J Med 2019;381:1632–43.

42. Abdel-Rahman WM, Katsura K, Rens W, Gorman PA, Sheer D, Bicknell D, et al. Spectral karyotyping suggests additional subsets of colorectal cancers characterized by pattern of chromosome rearrangement. Proc Natl Acad Sci U S A 2001;98:2538–43.

43. Kent LN, Leone G. The broken cycle: E2F dysfunction in cancer. Nat Rev Cancer 2019;19:326–38.

44. Kazi A, Xiang S, Yang H, Delitto D, Trevino J, Jiang RHY, et al. GSK3 suppression upregulates β-catenin and c-Myc to abrogate KRas-dependent tumors. Nat Commun 2018;9:5154.

45. Chang L, Jung NY, Atari A, Rodriguez DJ, Kesar D, Song TY, et al. Systematic profiling of conditional pathway activation identifies context-dependent synthetic lethalities. Nat Genet 2023;55:1709–20.

46. Dias MH, Fonseca CS, Zeidler JD, Albuquerque LL, da Silva MS, Cararo-Lopes E, et al. Fibroblast growth factor 2 lethally sensitizes cancer cells to stress-targeted therapeutic inhibitors. Mol Oncol 2019;13: 290–306.

47. Bermudez O, Pagès G, Gimond C. The dual-specificity MAP kinase phosphatases: critical roles in development and cancer. Am J Physiol Cell Physiol 2010;299:C189–202.

48. Unni AM, Harbourne B, Oh MH, Wild S, Ferrarone JR, Lockwood WW, et al. Hyperactivation of ERK by multiple mechanisms is toxic to RTK-RAS mutation-driven lung adenocarcinoma cells. eLife 2018;7:e33718.

49. Kong A, Mehanna H. WEE1 inhibitor: clinical development. Curr Oncol Rep 2021;23:107.

50. Fang Y, McGrail DJ, Sun C, Labrie M, Chen X, Zhang D, et al. Sequential therapy with PARP and WEE1 inhibitors minimizes toxicity while maintaining efficacy. Cancer Cell 2019;35:851–67.

51. Bukhari AB, Lewis CW, Pearce JJ, Luong D, Chan GK, Gamper AM. Inhibiting Wee1 and ATR kinases produces tumor-selective synthetic lethality and suppresses metastasis. J Clin Invest 2019;129:1329–44.

52. Chang KE, Wei BR, Madigan JP, Hall MD, Simpson RM, Zhuang Z, et al. The protein phosphatase 2A inhibitor LB100 sensitizes ovarian carcinoma cells to cisplatin-mediated cytotoxicity. Mol Cancer Ther 2015;14:90–100.

53. Lu J, Kovach JS, Johnson F, Chiang J, Hodes R, Lonser R, et al. Inhibition of serine/threonine phosphatase PP2A enhances cancer chemotherapy by blocking DNA damage induced defense mechanisms. Proc Natl Acad Sci U S A 2009;106:11697–702.

54. Kotsantis P, Petermann E, Boulton SJ. Mechanisms of oncogene-induced replication stress: jigsaw falling into place. Cancer Discov 2018;8:537–55.

55. Perera D, Venkitaraman AR. Oncogenic KRAS triggers MAPK-dependent errors in mitosis and MYC-dependent sensitivity to anti-mitotic agents. Sci Rep 2016;6:29741.

56. Littler S, Sloss O, Geary B, Pierce A, Whetton AD, Taylor SS. Oncogenic MYC amplifies mitotic perturbations. Open Biol 2019;9:190136.

57. van Neerven SM, de Groot NE, Nijman LE, Scicluna BP, van Driel MS, Lecca MC, et al. Apc-mutant cells act as supercompetitors in intestinal tumour initiation. Nature 2021;594:436–41.

58. Anmella G, Fico G, Lotfaliany M, Hidalgo-Mazzei D, Soto-Angona Ó, Giménez-Palomo A, et al. Risk of cancer in bipolar disorder and the potential role of lithium: International collaborative systematic review and meta-analyses. Neurosci Biobehav Rev 2021;126:529–41.

59. Subramanian A, Tamayo P, Mootha VK, Mukherjee S, Ebert BL, Gillette MA, et al. Gene set enrichment analysis: a knowledge-based approach for interpreting genome-wide expression profiles. Proc Natl Acad Sci U S A 2005;102:15545–50.

60. Germain PL, Lun A, Macnair W, Robinson MD. Doublet identification in single-cell sequencing data using scDblFinder. F1000Res 2021;10:979.

61. Stuart T, Butler A, Hoffman P, Hafemeister C, Papalexi E, Mauck WM, et al. Comprehensive Integration of single-cell data. Cell 2019;177: 1888–902.

62. Becht E, McInnes L, Healy J, Dutertre CA, Kwok IWH, Ng LG, et al. Dimensionality reduction for visualizing single-cell data using UMAP. Nat Biotechnol 2019;37:38–47.

63. Traag VA, Waltman L, van Eck NJ. From Louvain to Leiden: guaranteeing well-connected communities. Sci Rep 2019;9:5233.

64. Love MI, Huber W, Anders S. Moderated estimation of fold change and dispersion for RNA-seq data with DESeq2. Genome Biol 2014;15:550.

65. Fang Z, Liu X, Peltz G. GSEApy: a comprehensive package for performing gene set enrichment analysis in Python. Bioinformatics 2023; 39:757.

66. Xie Z, Bailey A, Kuleshov MV, Clarke DJB, Evangelista JE, Jenkins SL, et al. Gene set knowledge discovery with enrichr. Curr Protoc 2021;1:e90.

67. Andreatta M, Carmona SJ. UCell: Robust and scalable single-cell gene signature scoring. Comput Struct Biotechnol J 2021;19:3796–8.

68. Colic M, Wang G, Zimmermann M, Mascall K, McLaughlin M, Bertolet L, et al. Identifying chemogenetic interactions from CRISPR screens with drugZ. Genome Med 2019;11:52.